APPLIED SCIENCES AND ENGINEERING

Wireless, battery-free optoelectronic systems as subdermal implants for local tissue oximetry

Hao Zhang[1]*, Philipp Gutruf[1,2,3]*, Kathleen Meacham[4], Michael C. Montana[4], Xingyue Zhao[5,6], Antonio M. Chiarelli[7], Abraham Vázquez-Guardado[8], Aaron Norris[4], Luyao Lu[5], Qinglei Guo[5,9], Chenkai Xu[10], Yixin Wu[1], Hangbo Zhao[2], Xin Ning[5†], Wubin Bai[1,2], Irawati Kandela[11,12], Chad R. Haney[10,12,13], Debashis Chanda[8], Robert W. Gereau IV[4,14], John A. Rogers[15‡]

Monitoring regional tissue oxygenation in animal models and potentially in human subjects can yield insights into the underlying mechanisms of local O_2-mediated physiological processes and provide diagnostic and therapeutic guidance for relevant disease states. Existing technologies for tissue oxygenation assessments involve some combination of disadvantages in requirements for physical tethers, anesthetics, and special apparatus, often with confounding effects on the natural behaviors of test subjects. This work introduces an entirely wireless and fully implantable platform incorporating (i) microscale optoelectronics for continuous sensing of local hemoglobin dynamics and (ii) advanced designs in continuous, wireless power delivery and data output for tether-free operation. These features support in vivo, highly localized tissue oximetry at sites of interest, including deep brain regions of mice, on untethered, awake animal models. The results create many opportunities for studying various O_2-mediated processes in naturally behaving subjects, with implications in biomedical research and clinical practice.

INTRODUCTION

Regional tissue oxygenation reflects the balance between O_2 supply and demand and represents a ubiquitous hallmark in various physiological and pathological processes (*1*). Of particular interest are highly localized tissue oxygenation levels due to relevance in the interplay between O_2 dynamics and neural activity, tissue perfusion, tumor microenvironment, wound healing cascades, and many others, as shown by studies on small animal models (e.g., mice or rats) (*2*–*5*). Systems for reliable monitoring could lead not only to an improved understanding for O_2-mediated biological processes but also to important insights in clinical diagnostics and therapeutic guidance. Existing methods for the direct (in the form of O_2 partial pressure) or indirect (in the form of changes in the concentration of oxygenated hemoglobin, [HbO_2], and deoxygenated hemoglobin, [Hb]) assessments of localized tissue oxygenation in animal models have some combination of limitations associated with inability to operate at substantial depths beneath the body surface [near-infrared spectroscopy (NIRS) or cerebral oximeters], requirements for physical tethers (O_2 electrodes, optical fibers, or bulky head stages), and/or need for anesthetics or special apparatus [brain oxygenation level–dependent magnetic resonant imaging (BOLD-MRI) and electron paramagnetic resonant spectroscopy (EPR)] (*6*, *7*). These disadvantages can lead to confounding effects associated with altered oxygenation levels due to anesthesia (*8*) and/or with physical constraints (*9*, *10*) on the natural behaviors of animal models, and associated inability to perform studies during social interactions.

Here, we present a miniaturized, fully implantable, wireless oximetry system that consists of a filamentary measurement probe (cross-sectional area less than 400 μm × 200 μm) interfaced to a small electronic module (lateral dimensions of less than 1 cm^2 and thickness of 1 mm), with unique capabilities that overcome these challenges. The sensing filament includes high-performance optoelectronic components [microscale inorganic light-emitting diodes (μ-ILEDs) and a microscale inorganic photodetector (μ-IPD)]. The electronic module supports wireless power harvesting, circuit control, and data communication to external receivers. The sensing exploits well-known differences in the optical properties of HbO_2 and Hb to quantify local changes in their concentrations ($\Delta[HbO_2]$ and $\Delta[Hb]$) as a means to estimate regional tissue oxygen saturation levels [$rStO_2 \approx 100\% \times [HbO_2]/([HbO_2] + [Hb])$] in small tissue volumes defined by the illumination profiles at the tip end of the sensing filament. Wireless power harvesting via magnetic resonant coupling and data transmission by infrared (IR) communication use small-scale electronic designs as an important extension of recently developed implantable platforms for optogenetic modulation (*11*–*17*) and photometric measurements (*18*). The miniaturized form factors (with the injectable parts similar in sizes to those of other minimally invasive techniques), the lightweight construction (~80 mg), the mechanically compliant designs, and the biocompatible encapsulation materials facilitate implantation, minimize tissue damage, and provide potential capabilities in robust, chronic operation. These features support unique capabilities in continuous localized $rStO_2$ measurements from devices subdermally implanted in

[1]Department of Materials Science and Engineering, Northwestern University, Evanston, IL 60208, USA. [2]Center for Bio-Integrated Electronics, Northwestern University, Evanston, IL 60208, USA. [3]Department of Biomedical Engineering, University of Arizona, Tucson, AZ 85721, USA. [4]Department of Anesthesiology, Washington University School of Medicine, St. Louis, MO 63110, USA. [5]Department of Materials Science and Engineering and Frederick Seitz Materials Research Laboratory, University of Illinois at Urbana-Champaign, Urbana, IL 61801, USA. [6]State Key Laboratory of New Ceramics and Fine Processing and School of Materials Science and Engineering, Tsinghua University, Beijing 100084, China. [7]Institute of Advanced Biomedical Technologies and Department of Neuroscience, Imaging and Clinical Sciences, University G. D'Annunzio of Chieti–Pescara, Chieti 66100, Italy. [8]NanoScience Technology Center, Department of Physics and CREOL, The College of Optics and Photonics, University of Central Florida, Orlando, FL 32826, USA. [9]Department of Materials Science, Fudan University, Shanghai 200433, China. [10]Department of Biomedical Engineering, Northwestern University, Evanston, IL 60208, USA. [11]Developmental Therapeutics Core, Northwestern University, Evanston, IL 60208, USA. [12]Chemistry of Life Processes Institute, Northwestern University, Evanston, IL 60208, USA. [13]Center for Advanced Molecular Imaging, Northwestern University, Evanston, IL 60208, USA. [14]Washington University Pain Center, Washington University School of Medicine, St. Louis, MO 63110, USA. [15]Departments of Materials Science and Engineering, Biomedical Engineering, Neurological Surgery, Chemistry, Mechanical Engineering, Electrical Engineering and Computer Science, Simpson Querrey Institute and Feinberg Medical School, Center for Bio-Integrated Electronics, Northwestern University, Evanston, IL 60208, USA.
*These authors contributed equally to this work.
†Present address: Department of Aerospace Engineering, The Pennsylvania State University, University Park, PA 16802, USA.
‡Corresponding author. Email: jrogers@northwestern.edu

peripheral tissues and even in targeted regions of the deep brain in both anesthetized and awake, freely moving animal models, with the ability to monitor transient changes in oxygenation. Resultant capabilities open up possibilities for studying a broad range of O_2-mediated, location-sensitive processes on naturally behaving subjects for both biomedical research and clinical practice.

RESULTS

Design features

Figure 1A shows an exploded schematic illustration of a fully implantable oximeter of the type described above. The platform incorporates two functional modules: (i) an injectable filament for real-time $rStO_2$ sensing (in the golden dashed box); (ii) a thin, battery-free module that supports wireless power delivery and control, photodiode amplification and analog front end, and optical data communication (in the green dashed box). The sensing filament exploits optoelectronic designs typical of reflectance-mode, $rStO_2$ oximeters [e.g., NIRS (*19*, *20*)], with a pair of μ-ILEDs that emits, in a time multiplexed fashion, at complementary wavelengths tailored toward efficient measurement of [HbO_2] and [Hb] levels. A single photodiode measures the attenuated light backscattered by hemoglobin molecules in blood associated with the surrounding tissues and vasculature. The fabrication procedures represent extensions of those recently reported for wireless systems for optogenetic modulation (*11*–*17*) and photometric measurements (*18*). In brief, the techniques of microtransfer printing with elastomeric stamps [made from polydimethylsiloxane (PDMS)] enable precise assembly of two μ-ILEDs (with dimensions of 270 μm × 220 μm × 50 μm and 240 μm × 240 μm × 100 μm) and one μ-IPD (with dimensions of 100 μm × 100 μm × 5 μm) onto a substrate of polyimide (PI; thickness, 75 μm). Photolithographically defined traces of gold/copper (Au/Cu; width, 20 μm; thickness, 700 nm) form interconnects between these optoelectronic components.

Depending on application requirements, the two μ-ILEDs can be located on opposite or the same side as the μ-IPD, as shown in Fig. 1 (B and C). The former configuration exploits a dual-layered design with μ-ILEDs and μ-IPD separated by a 7-μm-thick, insulating layer of a photodefinable epoxy (SU-8; Fig. 1B). The supporting filament has a width of ~380 μm and a thickness of ~80 μm (~200 μm for the entire filamentary probe), with a length to match the application. These probes are comparable in cross-sectional area to those in conventional, tethered techniques for tissue O_2 measurements, such as fiber oximetry (e.g., diameters of ~250 μm) and polarography (e.g., diameters of 200 to 300 μm for O_2 electrodes) (*6*), and with traditional fibers used for optogenetics (outer diameters of 230 to 480 μm) (*21*, *22*). The low stiffness of the filaments [between two and three orders of magnitude smaller than those of typical optical fibers (*23*, *24*)] allows compliant mechanical interfaces with soft tissues, thereby reducing disruption due to implantation and chronic use. These collective features enable deployment of these systems for $rStO_2$ sensing at sites within sensitive tissues, including regions of the deep brain, in a wide range of animal models, including mice. The latter configuration includes two μ-ILEDs on the same side as the μ-IPD (Fig. 1C) and is most amenable to use outside the brain, especially in locations that require highly localized sensing of $rStO_2$.

In both cases, bioinert coatings (a conformal coating of parylene with a thickness of 14 μm and, in some cases, an additional coating of PDMS with a thickness of ~10 μm) encapsulate the devices as barriers to biofluids to ensure their stable operation as chronic implants. The efficacy of these coating materials has been evaluated on related functional implants in the brains of living animal models in previous reports (*14*, *18*, *25*). Detailed descriptions of the fabrication procedures appear in fig. S1 and in Materials and Methods. Figure 1 (D and E) shows photographs and scanning electron microscopy (SEM) images of representative filaments, highlighting their small dimensions, particularly those with the dual-layered design [Fig. 1, D (right) and E (top)]. For use cases that require the sensing unit to be separated from the electronic module by a relatively large distance, the filament can be formed into a long, serpentine-shaped geometry (length of ~4 cm for this example, but selectable over a wide range) (*26*) to maintain system-level functionality with a high degree of mechanical flexibility and stretchability [Fig. 1, E (bottom) and F]. Additional illustrations and images appear in figs. S2 and S3.

Integration of the injectable filament with the electronic module occurs through low-temperature reflow soldering to yield a functional system (Fig. 1G). The electronic module incorporates wireless power harvesting via magnetic resonant coupling to an external antenna and wireless data communication by IR broadcast to a collection of photoreceivers (Fig. 1H). The harvesting unit includes (i) a loop antenna optimized for an operation frequency of 13.56 MHz, with minimum sizes defined by areas of ~0.9 cm^2, with side lengths of ~1 cm, consisting of five turns of copper traces (widths and spaces of 70 μm), and (ii) a subsequent half bridge rectifier with a ceramic capacitor (4.7 μF) for waveform smoothing followed by a supercapacitor (2.2 mF) for buffering, as the basis for stable power supply at a voltage of 3 V through a low-dropout regulator (Fig. 1H, green dashed box). During operation, a low-power microcontroller (μC) defines the timing of activation/deactivation of the μ-ILEDs (in an alternating time-sequenced manner), the sampling of the transmitted signals via the integrated analog-to-digital converter (ADC), and the timing of the IR LED for wireless communication (carrier frequency, ~38 kHz).

A miniaturized analog front end conditions and amplifies the response of the μ-IPD to attenuated, backscattered light from μ-ILEDs. External integrated data receivers (illustrated in the blue dashed box in Fig. 1H) that incorporate automatic gain control, band-pass filtering, and demodulation yield digital signal data streams from IR light transmitted from the electronic module. The high IR transparency of biological tissues allows effective operation even with the electronic module fully implanted subdermally. An external μC analyzes and time-stamps these digital signals and sends them through a serial communication link to a personal computer for data storage and analysis. In addition to wireless power harvesting, the wireless electronic modules can also be designed to incorporate small, lightweight, polymer lithium ion batteries (fig. S4) (*18*). These lightweight (as small as <0.1 g; fig. S5), subdermal implants offer capabilities for probing localized $rStO_2$ at sites of interest in untethered animal models that lie outside of those possible with conventional technologies.

Optical and electrical characterizations

The estimation of $rStO_2$ relies on the distinct absorption spectra of hemoglobin in the visible and NIR spectral range, depending on their oxygenation forms (HbO_2 or Hb). In general, the ratio of HbO_2 in hemoglobin molecules tends to increase at elevated O_2 concentration but decreases under hypoxia. Figure 2A shows the molar extinction coefficient (ε) spectra of HbO_2 and Hb according to reported data (*27*). Substantial changes in the spectral dependence of ε occur during the transition between HbO_2 and Hb. The absorption spectra of hemoglobin solutions appear approximately as linear combinations of

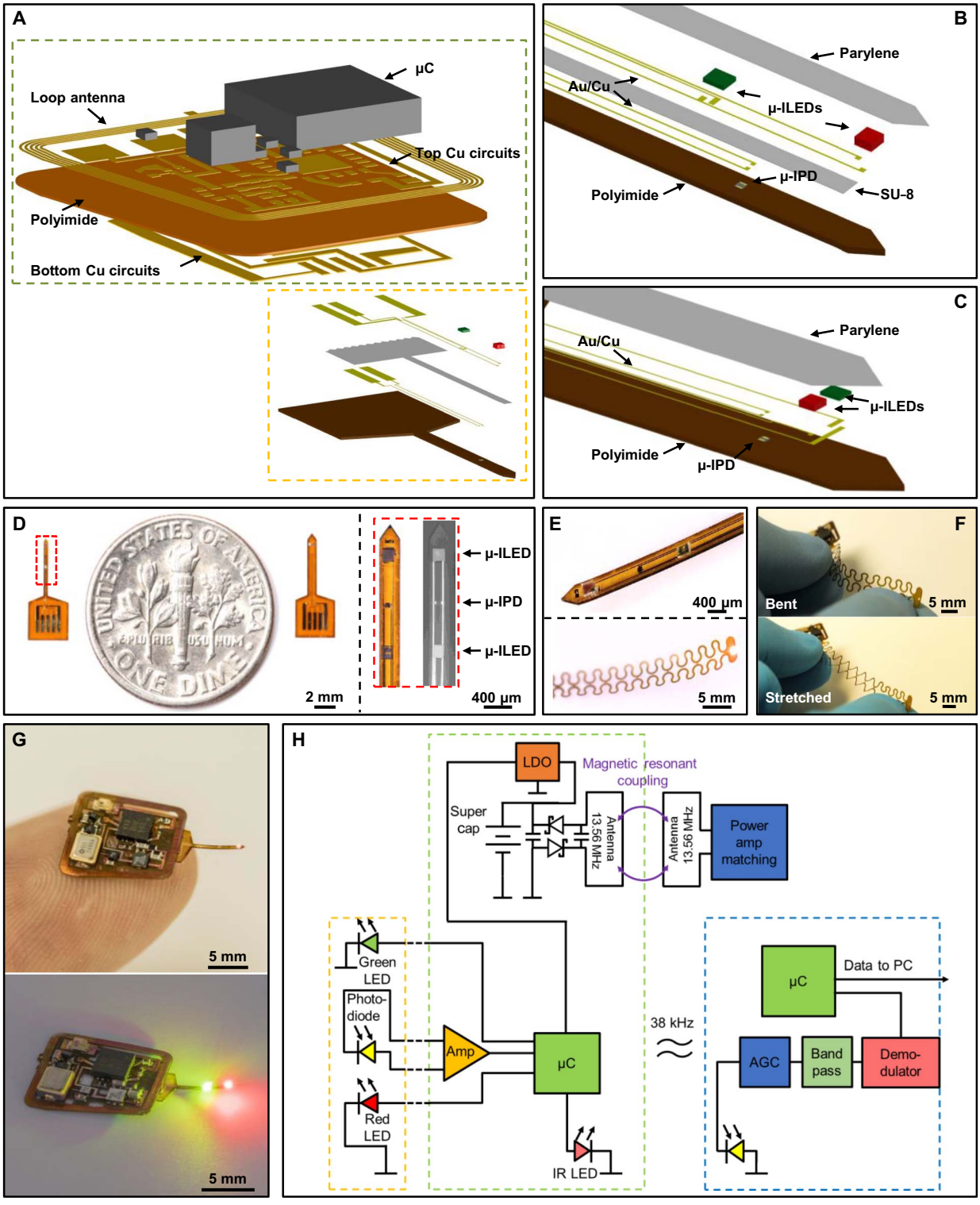

Fig. 1. Miniaturized, fully implantable, wireless oximeters for $rStO_2$ measurements. (**A**) An expanded view of the device platform including the electronic module (green dashed box; only parts of the electronic components are shown) and the injectable module (golden dashed box). (**B** and **C**) Schematic illustrations highlighting two representative filamentary designs: (B) dual-layered design for deep brain $rStO_2$ sensing of mice and (C) single-layered design for highly localized $rStO_2$ sensing in other tissue regions. (**D**) Left: Photograph of the dual- and single-layered filaments near a U.S. dime. Right: Optical and SEM images of the tip end of the dual-layered design (red dashed box in the left panel) with two μ-ILEDs placed as the opposite sides of the μ-IPD. (**E**) Photographs of (top) the dual-layered and (bottom) stretchable filamentary sensing modules at a tilted view. (**F**) Images of flexible and stretchable filaments with serpentine interconnects. (**G**) Integrated wireless, battery-free oximeters in operation mode with illuminating μ-ILEDs. (**H**) Block diagram of the electrical working principles. LDO, low-dropout regulator; AGC, automatic gain control; Supercap, supercapacitor. (Photo credit: Hao Zhang and Philipp Gutruf, Northwestern University)

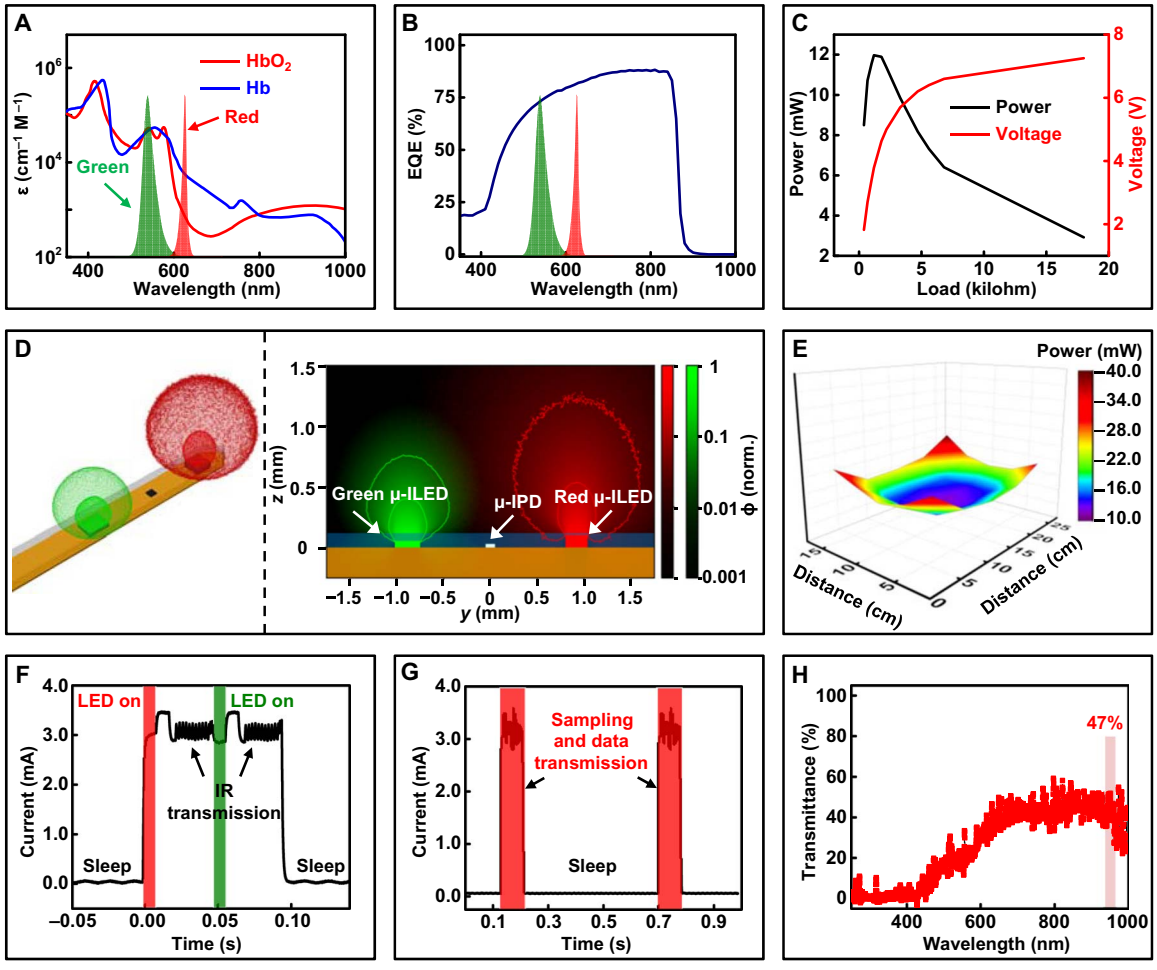

Fig. 2. Optical and electrical characterizations of wireless, battery-free implantable oximeters. (**A**) ε spectra of HbO_2 and Hb solutions. Green and red shaded areas indicate the emission spectra of corresponding μ-ILEDs. (**B**) EQE spectrum of μ-IPD, showing high responsivities in a wide spectral band covering the emission wavelengths of μ-ILEDs (shaded areas). (**C**) Rectifier characterization with increasing load at the center of an experimental area with the dimensions (25 cm × 15 cm × 10 cm) of a mouse home cage. The RF power input is 4 W. (**D**) Monte Carlo simulation of the spatial distribution of normalized emission intensity profiles from μ-ILEDs in a turbid medium replicating the optical properties of rodents' brain [left: three-dimensional (3D) rendering image; right: 2D plots with 10 and 1% contours of the initial emission intensities]. (**E**) Spatially resolved, available transmitted power in the experimental arena with the RF power input of 4 W. (**F** and **G**) Time-resolved current consumption profile of devices: (F) during a sampling (indicated by the red and green bars when the corresponding μ-ILED is on) and data transmission event and (G) over 1-s period with two cycles (highlighted by red bars) of sampling and data transmission. (**H**) Transmittance spectrum of mouse scalp with ~47% transmittance at the wavelength for IR data broadcast (950 nm).

those of HbO_2 and Hb as a function of $rStO_2$. The result correlates the $rStO_2$ (as a function of [HbO_2] and [Hb]) to measurable optical properties (i.e., light attenuation by hemoglobin under transmission or backscattering mode). Commercial $rStO_2$ oximeters that operate on the skin generally use LEDs with two or more wavelengths: (i) in the NIR regime (~700 to 850 nm) with relatively large penetration depths through skin related to the low ε of water and main chromophores in the skin, and (ii) below and above the isosbestic point (~800 nm) where the sensitivity to oxygenation of hemoglobin is high, due to considerable differences between ε(HbO_2) and ε(Hb) (*20*, *28*). By comparison, the geometry of the oximeter platform introduced here involves a short source-detector distance, thereby allowing the use of red- and green-emitting μ-ILEDs (625 nm with full width at half maximum of ~10 nm and 540 nm with full width at half maximum of ~30 nm, respectively; Fig. 2A) that are more well aligned to commercially available, small-scale components. The red μ-ILED allows probing the spectral range where the difference between ε(HbO_2) and ε(Hb) is large [ε(Hb)/ε(HbO_2) up to 10 in the range of 600 to 700 nm; fig. S6] to enhance the ability to measure Δ[HbO_2] and Δ[Hb]. The green μ-ILED, by contrast, probes a portion of spectrum where ε(HbO_2) and ε(Hb) are similar, thereby permitting evaluation of oscillations in the total hemoglobin concentration and elimination of the influence of an unknown background (*20*), which are insensitive to $rStO_2$ changes. Specifically, algorithms based on the modified Lambert-Beer law for diffusive media allow quantitative calculation of Δ[HbO_2] and Δ[Hb] and estimation of $rStO_2$ with priori approximations about the baseline values (Materials and Methods). Detection of attenuated backscattered light from both μ-ILEDs relies on a single μ-IPD with high sensitivity to visible light [external quantum efficiency (EQE), ~74% at 540 nm and ~82% at 625 nm; shown in Fig. 2B].

The fabrication of these custom μ-IPDs relies on GaAs-based epitaxial structures grown with precise control over the doping profiles (figs. S7 and S8) and follows from a series of steps in photolithography, etching, and microtransfer printing (*18*). Characteristics of the μ-ILEDs

and the μ-IPD, such as the current-voltage curves, appear in fig. S9. The distance between the μ-ILEDs and the μ-IPD, also known as the interoptode distance, sets the characteristic depth associated with backscattered light that arrives at the μ-IPD and strongly affects the signal-to-noise ratio. In general, increasing interoptode distance extends the optical path and enlarges the probing volume, which enhances the variations in signals due to changes in $rStO_2$. Increases in interoptode distance also, however, decrease the light detected by the PD due to strong absorption and scattering events that occur in turbid media (*29*), which ultimately increase the noise in the detected signals. The interplay between probing depth, sensing volume, and signal-to-noise ratio represents a challenge for conventional $rStO_2$ oximeters. By contrast, the injectable platforms presented here allow sensing in deep tissue regions at a small interoptode distance (700 μm) with adequate signal-to-noise ratio.

Monte Carlo simulations provide quantitative insights into the photon distributions around the μ-ILEDs and into aspects of light detection by the μ-IPD at this interoptode distance. The models use optical properties characteristic of those of mouse brain tissue. Details on these simulations appear in Materials and Methods. Figure 2C shows the normalized emission intensity profiles of green and red μ-ILEDs as a function of distance. The penetration depth, or the location where the optical intensity decreases to e^{-2} or ~10% of the initial value, is around 0.4 and 0.5 mm for the green and red μ-ILEDs, respectively. The characteristic sizes of the illumination volumes are ~0.5 to 2 mm^3 depending on the threshold light intensities (e.g., intensities at 10% or 1% of the initial values). The large absorption and scattering coefficients associated with brain tissue, the divergent illumination patterns of the μ-ILEDs, and the height differences between the μ-ILEDs and the μ-IPD lead to detected signals that are dominated by backscattered light, with little contribution (over five orders of magnitude lower compared to that from backscattered light, according to simulated data) from light that passes directly from the μ-ILEDs to the μ-IPD. On the basis of the measured EQE of the μ-IPD, the simulated photoresponses as a function of $rStO_2$ across the physiologically relevant range (fig. S10) correlate qualitatively with data from in vivo experiments, as shown in the following section.

Efficient wireless power harvesting and reliable data transfer are critical features of continuous monitoring of $rStO_2$ using the platforms described here. Resonant power transfer and stabilization schemes for chronic and robust operation of devices in optogenetics serve as inspiration for the approaches used here (*25*). Figure 2D shows the unregulated power output of the rectifier with increasing load in the center of an experimental arena with the dimensions of a typical mouse home cage and circumflexed with a dual-loop primary antenna ($L \times W \times H$ = 25 cm × 15 cm × 10 cm; scheme shown in fig. S11) at a height of 3 cm with a radiofrequency (RF) power input of 4 W. The optimal working voltage for this antenna/rectifier combination is around 4 V, yielding a power of around 12 mW, which is sufficient for device operation (peak power requirement of 9 to 10 mW buffered by the supercapacitor and average power requirement of ~2 mW). Spatially resolved measurements with a shunt resistance of 3.3 kilohms (comparable to the system load) show harvesting capabilities that exceed 30 mW at the corners of the cage and reach minimum values of around 12 mW at the center (Fig. 2E). The available power at any location within the cage exceeds that needed for stable voltage output of 3 V.

The average power required for robust device operation is further reduced by power management schemes shown in Fig. 2 (F and G), which illustrates the time-resolved current consumption of the system. These schemes feature (i) "sleep" phases (~80% of the operational time) where most of the μC peripherals are off to minimize current consumption levels (below a few tens of microamperes) and (ii) the sampling and data transmission phases (~20% of the operational time) where the power requirements are 9 to 10 mW. Using this operational duty cycle, the average power consumption drops to around 2 mW, which leaves ample margin for power supply even across large ($L \times W \times H$ = 30 cm × 30 cm × 20 cm) experimental enclosures. Here, brief bursts of data broadcast via IR at rates of over 27 Hz with 12-bit resolution. These rates far exceed those necessary to capture temporal variations in $rStO_2$ associated with tissue perfusion and global O_2 levels in animal models (well below 1 Hz) (*30*). As in recent work on wireless photometers (*18*), the IR data transmission scheme is stable even in non–line-of-sight scenarios when the millimeter-scale IR LED faces all cardinal directions in a mouse home cage equipped with external receivers at the corners. The use of IR, as opposed to a wavelength in the visible range, leads to minimal attenuation by tissues of animal models such as rodents. For instance, 950-nm IR light preserves ~47% of original intensity after passing through a piece of scalp from a sacrificed mouse (Fig. 2H and fig. S12).

Tests of wireless oximeters with artificial blood solutions

Basic evaluations of function of these wireless, battery-free devices use artificial blood solutions that contain different hemoglobin derivatives, as controlled simulations of in vivo assessments of $rStO_2$. Commercial bovine hemoglobin powders contain predominantly methemoglobin (metHb) with Fe(III) centers and readily form aqueous solutions in phosphate-buffered saline (PBS) (e.g., 25 g $liter^{-1}$, referred to as sol. 1 in Fig. 3A). This concentration is comparable to that of total hemoglobin in the peripheral blood and brain vascular systems of mice and rats (*31*, *32*). Adding excess reducing agents ($Na_2S_2O_4$, 8:1 in mass ratio to hemoglobin powders) to sol. 1 yields a solution with markedly increased absorbance at ~540 nm and reduced absorbance at ~625 nm (sol. 2 in Fig. 3A). The distinct optical absorption features of sol. 1 and sol. 2 result in substantial changes in detected photoresponses (as ADC values) associated with green (decreased by ~50% when switched from sol. 1 to sol. 2) and red (increased by ~40%) wavelengths, as measured by oximeters immersed in these solutions in plastic centrifuge tubes. Note that the output data are stable over time within ~±1.5% (fig. S13) when wirelessly powered by magnetic resonant coupling. These changes are negligible in amplitude compared to those associated with expected variations in hemoglobin compositions.

Figure 3B shows the computed ratios of output data ([ADC (green)/ADC(red)]) of five solutions with different compositions (absorption spectra shown in fig. S14), where sol. 1 and sol. 2 represent discrete oxygenation states of hemoglobin. These values correlate well with variations in optical absorbance of these solutions. Measurements of sol. 1 and sol. 2 at various locations (including center and corners) in an experimental arena of 25 cm × 15 cm × 10 cm reveal the system-level performance, including power harvesting, oxygenation measurements, analog front-end processing, and data communication, under conditions relevant to the context of $rStO_2$ measurements in freely moving animal models. The spatially resolved graph in Fig. 3C shows excellent stability of the ratios of output data associated with green and red wavelengths at different locations within the experimental arena (±2% to ±7% deviations, as represented by the error bars in Fig. 3B).

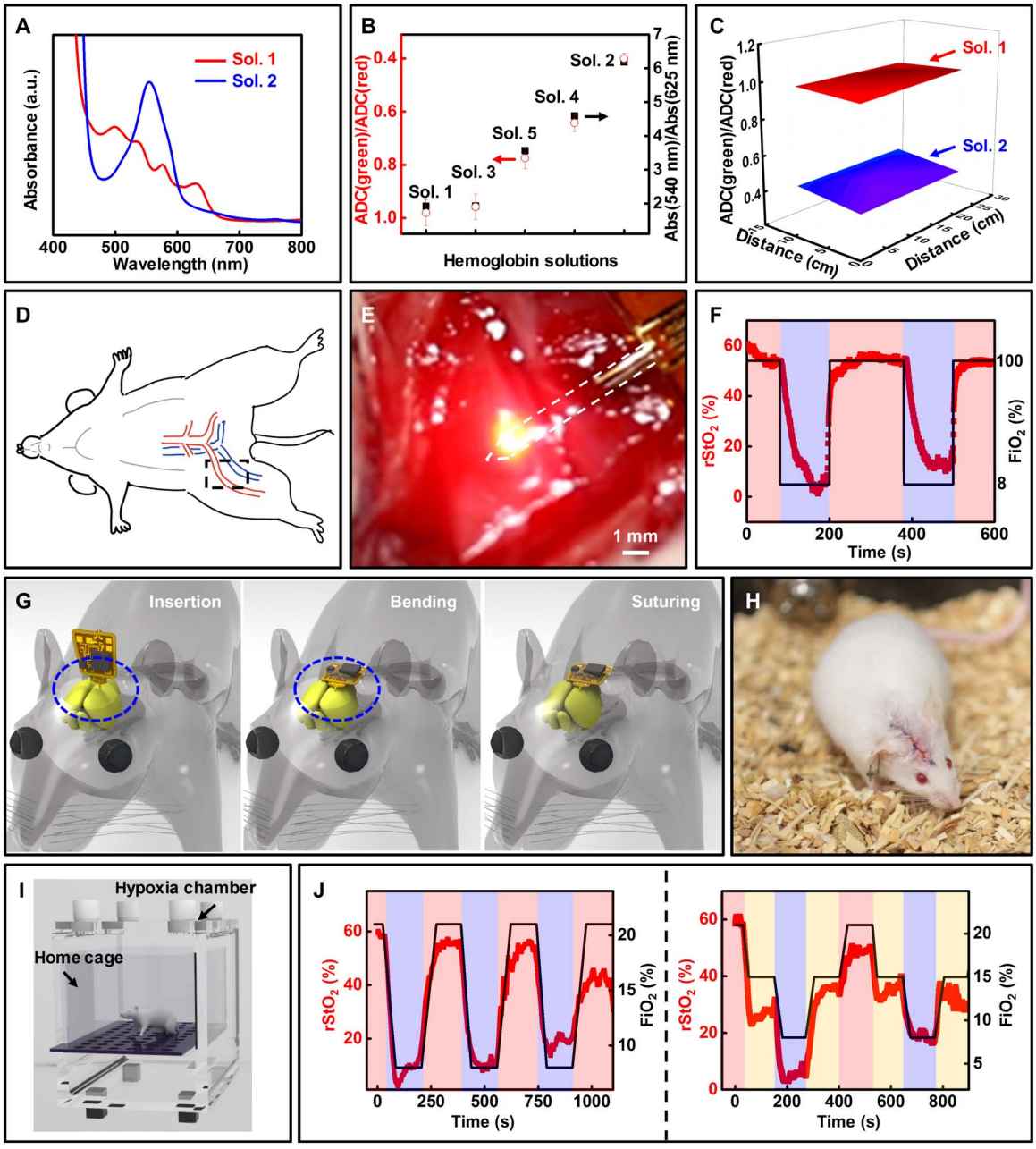

Fig. 3. Tests with artificial blood solutions and in vivo $rStO_2$ measurements on rodents. (**A**) Absorption spectra of two artificial blood solutions with different compositions. a.u., arbitrary units. (**B**) Correlation of the output photoresponse signals (red open circles; as the ratios of ADC values) from the wireless, battery-free oximeters, with the differences in optical absorbance [black solid squares; as the ratios of absorbance (Abs) at 540 and 625 nm] of five artificial blood solution samples. (**C**) Spatially resolved output signals of wireless oximeters measured from sol. 1 and sol. 2 at different locations in an experimental arena with the dimensions (25 cm × 15 cm × 10 cm) of a mouse home cage. (**D**) Scheme of an anesthetized rat highlighting the femoral artery and vein region (red and blue blood vessels, respectively). (**E**) Photograph of a wireless oximetry implant (battery-powered, with the injectable module outlined by white dashed lines) in the tissue region near the femoral artery of an anesthetized rat. (**F**) Estimated $rStO_2$ (red traces) in the tissue region [shown in (E)] of an anesthetized rat exposed to FiO_2 changes (black traces) between 100% (red blocks) and 8% (purple blocks). (**G**) Scheme of surgical steps of the subdermal implantation of wireless oximeters in mouse brain (yellow sections). Left to right: Insertion of the filament into the brain with opened scalp (circled by blue dashed lines) via a drilled hole; bending the electronic module followed by fixing it on skull; and closing the scalp with bioresorbable sutures. (**H**) Photograph of a freely moving mouse with subdermally implanted oximeter in the brain. (**I**) Schematic illustration of the setup for deep brain $rStO_2$ measurements of a freely moving mouse. (**J**) Estimated $rStO_2$ changes (red traces) in the deep brain region of freely moving mice in a hypoxia chamber with precisely controlled FiO_2 profiles (black traces; oscillating between 8 and 21%) using battery-powered oximeters. Changes in the color of blocks (red, yellow, and purple) indicate the time for FiO_2 changes. (Photo credit: Philipp Gutruf, Northwestern University)

In vivo $rStO_2$ measurements on anesthetized and freely moving rodents

These in vitro results establish the basis of in vivo assessments of localized $rStO_2$ with probes implanted at sites of interest in living animal models, without the physical constraints of tethered hardware required by other systems. Encapsulated battery-powered devices implanted near the femoral artery (as indicated in the scheme shown in Fig. 3D) of anesthetized rats operate effectively (Fig. 3E). With related types of devices (*14*, *18*, *25*), the parylene/PDMS encapsulation scheme can support stable operation as implants in mouse models for 1.5 years. These results suggest potential capabilities in chronic operation of devices reported here. As the anesthetized rats ($n = 4$ animals; total number of measurements = 10) experience oxygenation challenges via a nose cone [i.e., inspired fraction of O_2, FiO_2, varied between hyperoxia (100% O_2 with 2% isoflurane), hypoxia (8% O_2), and normoxia (ambient air)], $\Delta[HbO_2]$ and $\Delta[Hb]$ yield substantial changes in the measured data (fig. S15). For instance, decreased FiO_2 leads to reduced photoresponses associated with the red emission because $\Delta[HbO_2] < 0$ and $\Delta[Hb] > 0$. In comparison, the photoresponses from green light are less sensitive to oxygenation challenges (and thus $rStO_2$), consistent with the optical absorption features (Fig. 2A and fig. S6) and the simulated results (fig. S10).

These extracted photoresponses (in the form of ADC values) allow the quantitative calculation of $\Delta[HbO_2]$ and $\Delta[Hb]$ using algorithms and data processing strategies described in Materials and Methods, derived from a modified Lambert-Beer law for diffusive media. In brief, the methods include extracting high and low ADC values corresponding to the two operating wavelengths, low-pass filtering with a zero-lag digital Butterworth filter, and linear detrending to account for drifts of the raw data (e.g., fig. S15B). Compared to arterial blood oxygen saturation (SaO_2; another vital sign related to oximetry used in clinic practices), a critical challenge in the estimation of $rStO_2$ is the lack of a reliable "gold standard," as $rStO_2$ represents a weighted average of the oxygen saturation throughout all intravascular blood within the illuminated volume (*33*). Consequently, commercial $rStO_2$ oximeters are typically used to monitor trends with pooled root mean square errors of ~±8% and relatively large variations among human subjects (*19*, *33*). Despite these complications, the algorithm used here yields estimates of $rStO_2$ (Fig. 3F) with assumptions for the total concentration of hemoglobin (~150 g liter^{-1}) and the baseline value of $rStO_2$ (~60%) (*31*, *32*). The temporal changes in estimated $rStO_2$ coincide with the hyperoxia-hypoxia FiO_2 cycles, with fast temporal response. An interesting observation is that the data suggest that the vascular system in this tissue region is more resistant to the transition from hyperoxia to hypoxia than the other way around (Fig. 3F and fig. S15). Similar "asymmetric" changes appear in photoacoustic imaging of $rStO_2$ in the brains of anesthetized mice (*34*). Placing the same device at different distances (0.5 to 1 mm versus 2 to 4 mm) from the femoral artery of the same rat yields notable changes in the computed ratios of the output photoresponses (fig. S15C), likely due to spatial variations in $rStO_2$ (*35*).

Advanced demonstrations involve real-time cerebral oximetry in the striatum of untethered, freely moving mice, as an example of a capability that would be difficult or impossible to replicate with existing direct or indirect O_2 measurement technologies. Subdermal implantation of miniaturized, wireless, battery-free oximeters (Fig. 1G) in the mouse brain follows stereotactic surgical procedures described in previous reports (*14*, *18*, *25*). Figure 3G illustrates some of these steps, beginning with lowering the filament into a hole drilled at desired coordinates of the brain through the exposed skull, followed by fixing the probe with dental cement or cyanoacrylate to minimize relative movements in the brain (Fig. 3G, left), bending the electronic module and fixing it onto the skull (Fig. 3G, middle), and finally closing the scalp with bioresorbable sutures (Fig. 3G, right). Details appear in fig. S16. These fully implantable embodiments show reliable operation and continuous data recording capabilities throughout a mouse home cage circumflexed with a dual-loop primary antenna, thereby allowing measurements of $rStO_2$ in deep brain regions of awake, freely moving mice (fig. S17). The implants introduce minimal injury to the brain during the surgery, and they prevent postoperative hindrances in the natural movements (Fig. 3H), as also evidenced in previous reports deploying related devices in optogenetic studies of mouse brain (*14*, *25*). Mice implanted with battery-powered devices also show few changes in locomotor behaviors or social interactions (fig. S18), consistent with observations in adult mice using devices with similar weights (~0.5 g) and dimensions (*18*). Placing freely moving mice implanted with battery-powered devices ($n = 3$; total number of measurements = 9) in a hypoxia chamber (illustrated in Fig. 3I) with precise control over FiO_2 (from 8% to about 21%) enables the continuous monitoring of cerebral $rStO_2$ in deep brain regions (striatum). Figure 3J shows the calculated $rStO_2$ during the FiO_2 challenges of 21%-8%-21%-8%-21%-8%-21% and 21%-15%-8%-15%-21%-15%-8%-15%, respectively. The total concentration of hemoglobin and the baseline $rStO_2$ at normoxia are assumed to be 0.1 mM liter^{-1} and 60% based on reported values (*32*, *36*). The $rStO_2$ levels do not completely recover to the baseline values (i.e., 60%) in 2 to 3 min after restoring FiO_2 in the hypoxia chamber from 8 to 21%, possibly due to vasoconstriction of microvessels of mouse brain in response to severe hypoxia (*35*, *37*).

As with other invasive O_2 measurement technologies, implantable oximeters can cause tissue damage during and after the implantation, especially in delicate regions of the anatomy such as the brain. Immunohistochemical analyses of slices of mouse brains collected 4 weeks after implantation (at the location of 2 mm lateral and 4 mm deep to bregma; Fig. 4, A and B) reveal the effects. The small size, the compliant mechanics, and the biocompatible encapsulation of the filamentary sensors minimize tissue displacements and show normal immunoglial response, as demonstrated in Fig. 4C. The estimated lesion sizes (360 μm × 240 μm) match the dimensions of the probes and are comparable to those of implants used in other O_2 measurement techniques (e.g., diameter of ~250 μm for fiber oximetry and 200 to 300 μm for O_2 electrochemistry). The battery-free implants reported here are also compatible with conventional imaging technologies such as micro–x-ray computed tomography (microCT). Despite certain device-induced artifacts, rendered images from slices in different orientations provide important insights on the location of the implants and the state of surrounding bones postoperatively, as shown in Fig. 4D. The sagittal (Fig. 4D, left) and coronal (Fig. 4D, right) views suggest that the electronic module laminates well on the skull where the small hole in the right panel corresponds to the location of the implantable filament. The relatively small extent of damage leads to minimal interruptions on the natural activities of mice, as suggested by the postoperative weight changes in a long term up to about 250 days (fig. S19).

DISCUSSION

The ultraminiaturized, lightweight optoelectronic platforms presented here enable continuous, highly sensitive, and localized $rStO_2$ sensing at sites of interest in untethered, awake animal models. The use of RF-

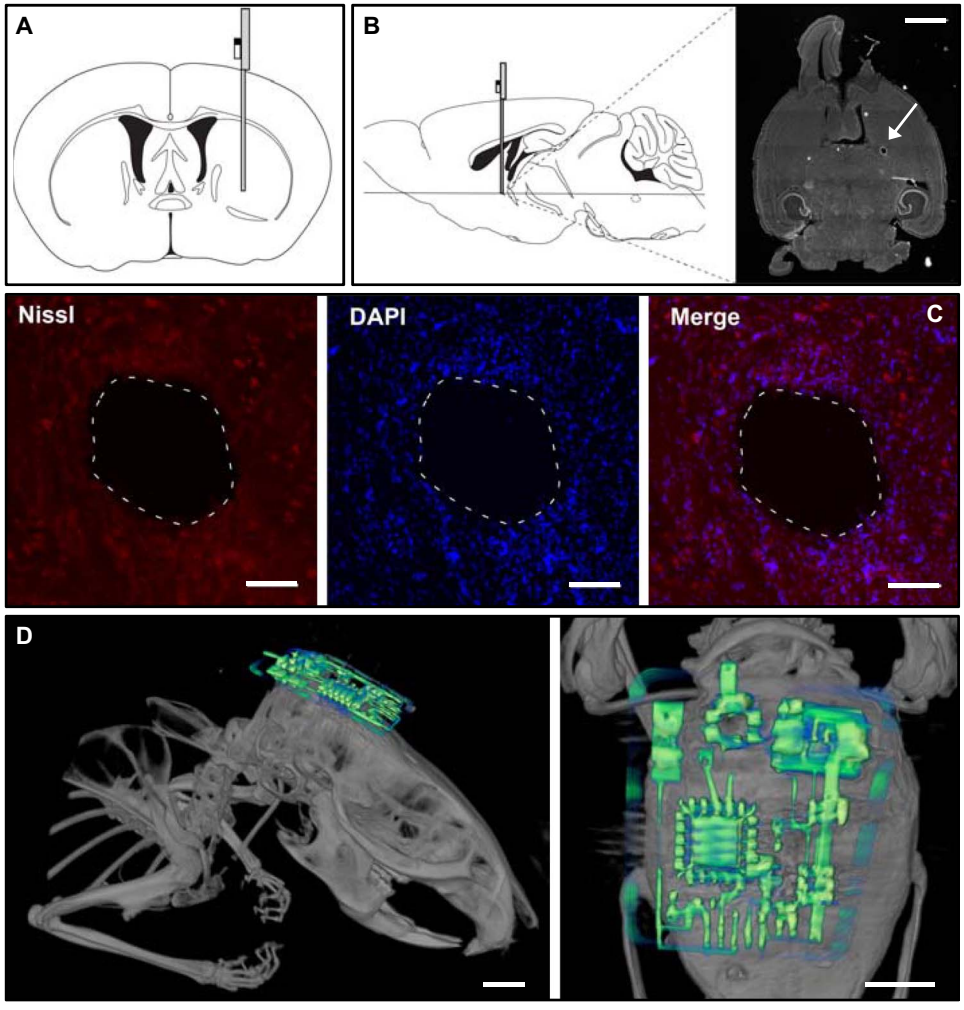

Fig. 4. Survey of location and tissue damage associated with wireless oximetry implants in the mouse brain. (**A** and **B**) Schematic and microscopic images of a representative mouse brain at the point of observation of tissue damage for lesion measurements. Scale bar, 2 mm (B). (**C**) Representative fluorescence images of horizontal striatum slices demonstrate lesion size (~360 μm × 240 μm) by immunohistochemical staining of neurons [Nissl, red; 4′,6-diamidino-2-phenylindole (DAPI), blue]. Scale bars, 100 μm. (**D**) 3D rendered microCT images of mice with battery-free, subdermal oximetry implants (highlighted in green color) in the brain. Scale bars, 3 mm.

based wireless power harvesting strategies and IR-based wireless data communication schemes allows deployment as subdermal oximetry implants for animal model studies without interruptions to natural behaviors. In addition, the mechanically compliant and biochemically inert designs avoid noticeable lesions or adverse immune responses, even when deployed in delicate regions of the brain.

The enabled capabilities for $rStO_2$ monitoring in targeted regions of deep tissues with millimeter-scale probing volumes complement those of conventional technologies (NIRS or cerebral oximeters, mostly for global or systemic $rStO_2$ measurements) that involve large form factors, limited probing depths (up to ~1 cm deep from the skin surface), and relatively large probing volumes (in the order of several to tens of cubic centimeters) (*20*, *38*). These features are also distinct from those provided by recently developed thin, skin-mounted (pulse) oximetry platforms that exploit flexible mechanical designs and high-performance organic (*39*–*41*) or inorganic optoelectronic components (*28*, *29*). The results create new possibilities for studying a broad range of O_2-mediated physiological and pathological processes in animal models, with potential for human translation. Examples include investigating function in specific regions of the brain using localized O_2 changes as surrogates of neural activity (*32*, *42*–*44*), targeting of tumors via their association with hypoxia environments and low $rStO_2$ (*3*, *45*), and postoperative (multisite) monitoring of tissue transplantation (e.g., flap reconstruction) where the early detection of compromised circulation in the form of low $rStO_2$ is critical (*46*, *47*). For instance, these oximetry implants, either in the free-standing formats or mounted on conventional biopsy needles, can guide tumor targeting in specific regions by providing location-sensitive $rStO_2$ values in real time. This approach has the potential to reduce the chance of erroneous tumor targeting, especially for tumor tissues with very small sizes. Other direct or indirect O_2 measurement technologies for examining these processes involve physical tethers [e.g., bulky head stages (*9*) or electrodes with diameters of a few hundred micrometers (*10*, *48*) for O_2 electrochemistry] or require specialized supporting equipment [e.g., EPR or BOLD-MRI equipped with magnetic fields of ~10 millitesla to multitesla (*6*); applicable only on anesthetized subjects]. In comparison, the devices demonstrated here favor $rStO_2$ measurements in freely moving animals without interruptions of their natural behaviors, especially in the context of social activities (*10*).

The fabrication concepts and electronic designs introduced here can also be leveraged to enable implantable platforms with other functionalities. The programmable electronic designs allow μ-ILED modulation and data recording at high frequencies (~100 Hz), with potential applicability to tracking of heart rate and heart rate variability in small animal models (e.g., rats or mice, up to ~10 Hz) with optimization in signal-to-noise ratios and measurement schemes, an important physiological parameter and indicator of stress and other external stimuli in behavioral studies (*49*). Moreover, although the results shown here involve a single combination of two wavelengths (green and red), the designs are compatible with a variety of μ-ILEDs with other emission colors and with μ-IPDs that have spectral selective sensitivities, allowing ratiometric or photometric analysis of important biomarkers [e.g., Ca^{2+} or cancer biomarkers such as microRNA (*50*)] or physiological parameters. Other extended options include the integration of the oximeter probes with other functional modules for optogenetic modulation or microfluidic drug delivery. These multimodal systems with colocalization of stimuli and oxygenation detection could support unique capabilities in coupling the metabolism of specific tissue regions with external physiological or pathological challenges.

MATERIALS AND METHODS

Fabrication of μ-IPDs

The fabrication of μ-IPDs involved a series of photolithographic and etching steps on GaAs-based epitaxial materials (purchased from Masimo Semiconductor Inc.) with precise control over dopant levels in each layer [from top to bottom: n-type, Te-doped GaAs top contact layer (100 nm, $>1 \times 10^{19}$ cm^{-3}); n-type, Si-doped GaAs top contact layer (100 nm, $\sim 2 \times 10^{18}$ cm^{-3}); n-type, Si-doped $In_{0.5}Ga_{0.5}P$ window layer (25 nm, 2×10^{18} cm^{-3}); n-type, Si-doped GaAs emitter layer (100 nm, 2×10^{18} cm^{-3}); p-type, Zn-doped GaAs layer (2500 nm, 1×10^{17} cm^{-3}); p-type, Zn-doped $Al_{0.3}Ga_{0.7}As$ back surface field layer (100 nm, 5×10^{18} to 1×10^{19} cm^{-3}); p-type, Zn-doped GaAs bottom contact layer (300 nm, 5×10^{19} cm^{-3}); $In_{0.5}Ga_{0.5}P$ window layer (700 nm); $Al_{0.95}Ga_{0.05}As$ release layer (500 nm); and GaAs substrate/handling layer; see fig. S7]. Similar fabrication procedures appear in a recent report (*18*). First, photolithography with AZ nLoF 2070 negative tone photoresist (Integrated Micro Materials; spin-coated at 3000 rpm; developed with AZ MIF 917 Developer), followed by electron beam evaporation of a bilayer of Cr/Au (10 nm/150 nm), defined the n-contacts. Using Cr/Au metal contacts as masks, a mixture of H_3PO_4 [85 weight % (wt %) in H_2O and 99.99% trace metal basis; Sigma-Aldrich], H_2O_2 (30 wt % in H_2O; ACS reagent, Sigma-Aldrich), and H_2O with a volumetric ratio of 3:1:25 removed the exposed n-type, Te- and Si-doped GaAs layers. After defining the n-type regions of the μ-IPDs by photolithography with SPR v3.0 (MicroChem; spin-coated at 3000 rpm; developed with AZ MIF 917 Developer), the n-doped $In_{0.5}Ga_{0.5}P$ window layer and GaAs p-n junctions in the p-regions and other regions without photoresist were removed by HCl (37%; ACS reagent, Sigma-Aldrich)/H_3PO_4 (1:1, v/v) and $H_3PO_4/H_2O_2/H_2O$ (3:1:25), respectively. Formation of the p-contacts (a bilayer of Cr/Au, 10 nm/150 nm) followed procedures similar to those for the n-contacts. Subsequent etching of heavily doped, p-contact layers (by $H_3PO_4/H_2O_2/H_2O$, 3:1:25) and intrinsic $In_{0.5}Ga_{0.5}P$ window layers (by HCl) in selected areas (i.e., those uncovered by photocured SPR v3.0) yielded isolated arrays of μ-IPDs (each with a dimension of 100 μm × 100 μm). Last, undercut etching of the $Al_{0.95}Ga_{0.05}As$ release layer by diluted hydrofluoric acid (HF) (HF/ethanol, 1:1.5) formed μ-IPDs in suspended configurations while tethered to the GaAs substrates via photopatterned, breakable polymer anchors.

Fabrication of injectable sensing filaments of oximeters

The fabrication followed procedures reported elsewhere (*18*) with some modifications. The fabrication of dual-layered, thin (width, ~380 μm) injectable filaments (fig. S1) started with lamination of a thin layer of PI (75 μm thick, Kapton, Fralock) onto a glass substrate (thickness, 1 mm) coated with PDMS (Sylgard 184, Dow Corning; part A/B, 10:1 in weight). A spin-cast PDMS layer (3000 rpm), after being fully cured, served as an adhesive layer between PI and glass. A PDMS stamp with relief structures enabled the microtransfer printing of a single μ-IPD from the growth substrate to the PI substrate coated with an adhesive layer with optimized formula (*51*) [prebaked at 100°C for 7 min before the transfer printing and cured at 100°C under ultraviolet (UV) irradiation, ~10 mW cm^{-2}, for up to 1 hour]. With the μ-IPDs as the masking layers, reactive ion etching [March RIE; pressure, 200 mtorr; power, 100 W; oxygen gas, 20 standard cubic centimeters per minute (sccm)] removed excessive adhesive materials and residues from the photoresist anchors. A 2-μm-thick photodefined layer of epoxy (SU-8 2002, MicroChem; spin-coated at 3000 rpm; developed with SU-8 Developer) then encapsulated the μ-IPD, leaving the p- and n-contact regions exposed. Subsequently, photolithography with AZ nLOF 2070 and liftoff with acetone defined the geometries of the metal interconnects (sputter-deposited layers of Cr/Au/Cu/Au/Cu/Au, 10/150/150/150/150/100 nm) and completed the fabrication of the μ-IPD layers. A photocured coating of epoxy (~7-μm-thick, SU-8 2007, MicroChem; spin-coated at 3000 rpm; developed with SU-8 Developer) encapsulated the μ-IPD layer before the fabrication of the metal interconnects (sputter-deposited layers of Cr/Au/Cu/Au/Cu/Au, 10/150/150/150/150/100 nm) for the μ-ILEDs. Laser-cutting (LPKF4 UV laser system) defined the shapes of the probes and microtransfer printing delivered the μ-ILEDs (green, C527TR2227 from Cree Inc.; red, AEHRAX10 from Epistar) to the desired locations. An In-Ag alloy solder (Indalloy 290, Indium Corporation) enabled robust mechanical and electrical contacts between the pads of the μ-ILEDs and the sputtered interconnects by heating at 150°C for 2 min during the microtransfer printing process (*18*). The resulting injectable filaments with dual-layered structure were then integrated with the electronic modules by low-temperature reflow soldering or via connectors (503480-0500, Molex LLC) for devices powered by magnetic resonant coupling and batteries, respectively. Chemical vapor deposited layers of parylene (~14 μm) and an optional dip-coated layer of PDMS (thickness, ~10 μm) encapsulated the systems. Fabrication of injectable filaments/probes with other configurations followed similar procedures. The single-layered probes used metal interconnects for the μ-IPD and the μ-ILEDs sputter deposited on the same layer. The fabrication of probes with stretchable, serpentine-shaped interconnects included a spin-coated and cured layer of PI (thickness, ~5 μm) on top of the metal interconnects. This design placed the interconnect close to the neutral mechanical plane for strain reduction. Photolithographic patterning and reactive ion etching of the top PI layers in selected regions exposed the contacts.

Fabrication of electronic modules of wireless, battery-free oximeters

Fabrication of the electronic modules followed methods described elsewhere (*25*). Critical components included a μC (ATtiny84A, 3 × 3 mm package, Atmel), Schottky diodes for efficient power harvesting

(SMS7621-060, Skyworks Solutions Inc.), zero-input crossover distortion amplifiers (ADA4505-2, Analog Devices), and a small footprint IR LED for data communication (SFH 4043, 0402 package, Osram Opto Semiconductors Inc.). In addition, introduction of a supercapacitor (CPH3225A-2K, Seiko) buffered the harvested power to maintain a reliable, stable voltage supply during data transmission and sampling.

Characterizations of optoelectronic and electronic components of oximeters

The current-voltage curves of μ-ILEDs and μ-IPDs were measured by a Keithley 2400 source meter. The light source for characterizing the μ-IPDs was an Oriel 91192 solar simulator with an AM 1.5G filter and a power density of 100 mW/cm^2. The EQE spectra of the μ-IPDs were collected using a halogen lamp coupled to a monochromator. The output intensities from the IR LEDs used for data communication (dominant wavelength at 950 nm; driving current of 10 mA) were measured using an optical power meter (PM200, Thorlabs), before (3.2 mW) and after (1.5 mW) passing through a piece of mouse scalp. The transmittance spectra of a plastic container (labeled as "reference" in fig. S12) and a piece of mouse scalp enclosed in the plastic container (labeled as "scalp" in fig. S12) were collected using a fiber optical spectrometer (Ocean Optics) with electric dark correction and integration time set as 0.01 and 12 s, respectively. With this set of integration time, scalp and reference show similar levels of transmission in the spectral band of ~700 to 1000 nm. The IR transmittance (~47% at 950 nm) measured by the optical power meter and the spectral information collected by the fiber optical spectrometer defined the transmittance spectra of the scalp shown in Fig. 2H.

Tests of oximeters with artificial blood solutions

The artificial blood solutions consisted of commercial hemoglobin powders from bovine blood (H2500-5G, Sigma-Aldrich; molecular weight, ~64,500; predominantly metHb) dissolved in 1× Dulbecco's PBS (J67802, Alfa Aesar; ~137 mM NaCl, ~2.7 mM KCl, ~1.47 mM KH_2PO_4, and ~8 mM Na_2HPO_4) in the presence of different reducing agents (ascorbic acid, A5960-25G, Sigma-Aldrich or sodium hydrosulfite with the formula of $Na_2S_2O_4$, 33381, Alfa Aesar). Adding excess amounts of $Na_2S_2O_4$ ($Na_2S_2O_4$/metHb, 1:4, 1:1, and 8:1, in mass ratio) to metHb solutions (25 g liter^{-1}; corresponding to sol. 1 in Fig. 3, A to C) formed solutions with features like those of a mixture of HbO_2 and Hb (e.g., sol. 2 in Fig. 3, A to C). Varying the types and contents of reducing agents led to artificial blood solutions (solution 1: metHb; solution 2: $Na_2S_2O_4$/metHb, 8:1; solution 3: ascorbic acid/metHb, 1:1; solution 4: $Na_2S_2O_4$/metHb, 1:1; solution 5: $Na_2S_2O_4$/metHb, 1:4; Fig. 3 and fig. S14) with different optical absorption spectra, as collected by a Cary 5000 UV-Vis-NIR spectrometer. Oximeters with probes immersed in these solutions recorded the photoresponses associated with green and red wavelengths (in the form of ADC values) for each solution.

In vivo $rStO_2$ measurements on anesthetized rats

In vivo $rStO_2$ measurements in tissue regions near the femoral artery used anesthetized, Sprague-Dawley rats. All procedures complied with the National Institutes of Health standards and were approved by the Animal Care and Use Committee of Washington University in Saint Louis. Rats were anesthetized with 2% isoflurane in a standard induction chamber and maintained at 2% via a nose cone after being transferred to a warm operation platform (37°C). Removing the hair near the left femoral region exposed the tissues, followed by incisions made in the proximity of femoral artery (typically right below the femoral artery at 0.5 to 1 mm). The probe part of battery-powered implantable oximeters was placed in the incision, while the electronic part remained laminated on the tissue surface and fixed with tapes and paraffin films. The $rStO_2$ measurements started after equilibrium at hyperoxia (~100% O_2 with 2% isoflurane) for 5 to 10 min and included oxygenation challenges with FiO_2 cycled between hyperoxia and hypoxia (8% O_2). The data recording ended with the hyperoxia states and, in some cases, involved an additional session of normoxia (room air). The data collection involved sampling alternating output levels (in the form of ADC values) corresponding to red and green light from μ-ILEDs at 25 Hz, followed by offline data analysis (via MATLAB R2016b, The MathWorks Inc.).

In vivo $rStO_2$ measurements on freely moving mice

In vivo $rStO_2$ measurements of freely moving mice with battery-powered devices used C57B16 mice (age, 12 weeks). The mice were group-housed before the implantation and thereafter individually housed. Implantation of battery-powered devices in the brains of mice followed reported procedures (*18*) except for the location (2 mm lateral and 4 mm deep to bregma). All procedures complied with the National Institutes of Health standards and were approved by the Animal Care and Use Committee of Washington University in Saint Louis. One day after recovery from surgery, freely moving, awake mice with implanted oximeters were transferred to a hypoxia chamber (Coy Laboratory Products, Grass Lake, MI) with precise control over FiO_2 levels. The $rStO_2$ measurements began with equilibrium at normoxia for about 5 min, followed by cycles of FiO_2 (continuous changes in FiO_2 between 21, 15, and 8%) in different sequences. Under hypoxia, mice showed less frequent movements and increased respiratory rates, with recovery to natural behavior and movements under normoxia. Data collection (25 Hz) and analysis followed procedures similar to those for anesthetized rats.

In vivo experiments on freely moving mice with battery-free, subdermally implantable oximeters used 30 to 40 g of CD1 IGS mice [Crl:CD1(ICR)] and involved procedures approved by the Institutional Animal Care and Use Committee (IACUC) of Northwestern University's program for the human care and use of animals. The IACUC also inspects the animal facilities and investigator laboratories. Evaluation of the implanted devices was performed in compliance with Animal Welfare and Northwestern's IACUC regulations. Sterilized devices (autoclaved) were implanted into the right striatum of anesthetized mice using methods described in a previous report (*25*). In the proximity of a mouse home cage equipped with a dual-loop primary antenna and connected to a commercial RF transmission system designed for optogenetics (Neurolux Inc.), the subdermally implanted oximeter remained operational in anesthetized and in awake, freely moving mice, with data streams consistent with those obtained benchtop experiments in terms of acquisition rate and signal quality. Analysis of the output timing on the bench and in the animal is shown in table S1.

Immunohistochemistry studies of brain tissues after device implantation

After a 4-week recovery period following brain surgery, mice with implanted oximeter devices were euthanized with pentobarbital sodium and intracadially perfused with 4% paraformaldehyde in PBS. The processing of sacrificed mouse brains included dissection, postfixation at 4°C for 24 hours, and cryoprotection in 0.1 M PBS (pH 7.4) containing 30% sucrose at 4°C for >24 hours. Brains were then cut into 30-μm sections and washed in PBS two to three times before being blocked in a blocking buffer (PBS containing 0.5% Triton X-100 and

5% normal goat serum) for 1 hour and then in Neurotrace 530/615 red fluorescent Nissl stain (1:400), followed by three washes in PBS and three washes in phosphate buffer. Last, the brain sections were mounted on glass slides with VECTASHIELD HardSet (Vector Labs) with a DAPI (4′,6-diamidino-2-phenylindole) filter. All sections were imaged on an epifluorescent microscope.

Monte Carlo simulation on the optical characteristics of oximeters

Monte Carlo simulations defined the spatial illumination profiles associated with operation of the μ-ILEDs and photoresponses of the μ-IPDs due to changes in $rStO_2$, for scattering and absorptive media with optical properties similar to those of brain tissues. The simulations used a three-dimensional volume with 500^3 bins of 10 μm size. For each simulation, an average of 6.5×10^6 photons were launched from rectangular light sources, 240 μm × 240 μm and 270 μm × 220 μm for the red and green μ-ILEDs, respectively, with 120° full divergence angle. The μ-IPD has a surface area of 100 μm × 100 μm. With this stochastic photon propagation method, the estimated optical power/photoresponse was calculated for different $rStO_2$ at two wavelengths. The absorption coefficients [$\mu_a(\lambda)$] as a function of $rStO_2$ are given by the following equation (*52*, *53*)

$$\mu_a(\lambda) = \ln 10 \cdot \left(\frac{[\mathrm{Hb}]_t}{M_\mathrm{W}} \left(\mathrm{rStO_2} \cdot \varepsilon_{\mathrm{HbO_2}}(\lambda) + (1 - \mathrm{rStO_2}) \cdot \varepsilon_{\mathrm{Hb}}(\lambda) \right) + W \mu_\mathrm{W}(\lambda) \right) \quad (1)$$

where $[\mathrm{Hb}]_t$ is the total concentration of hemoglobin, M_W is the molecular weight of hemoglobin (64,500 g mol^{-1}), W is the water content (%), and $\mu_\mathrm{W}(\lambda)$ is the absorption coefficient of water. The $\varepsilon(\lambda)$ of HbO_2 and Hb, and $\mu_\mathrm{W}(\lambda)$ are available from (*27*). Following from a previous report (*32*), the simulation set $[\mathrm{Hb}]_t$ to 10 g $liter^{-1}$ (~0.1 mM) and W to 65% and swept $rStO_2$ from 10 to 60%, relevant to the range of calculated $rStO_2$ for in vivo experiments. For each μ-ILED, wavelength-averaged absorption coefficients [$\mu_{a-\mathrm{LED}}(\lambda)$] accounted for dispersion in the emission spectra, using the following equation, where Δλ is the full width at half maximum of the corresponding normalized LED emission spectrum (ζ_LED)

$$\mu_{a-\mathrm{LED}}(\lambda) = \frac{1}{\Delta\lambda} \int \mu_a(\lambda) \zeta_\mathrm{LED}(\lambda) d(\lambda) \quad (2)$$

The scattering coefficient [$\mu_s(\lambda)$] at the dominant emission wavelength was calculated using the following equation (*53*)

$$\mu_s(\lambda) = a \frac{\left(\frac{\lambda}{500}\right)^{-b}}{1 - g} \quad (3)$$

where a is a scaling coefficient, b is the scattering power, and g is the anisotropy factor. For simulation in rodent's brain (a = 21.4 cm^{-1} and b = 1.2), the calculated μ_s(540 nm) = 195.2 cm^{-1} (g = 0.89) and μ_s(625 nm) = 163.2 cm^{-1} (g = 0.90). In comparison with $\mu_a(\lambda)$, which decreased with elevated $rStO_2$, $\mu_s(\lambda)$ remained constant in the course of the simulation.

To roughly estimate the contribution of photoresponses from light that passes directly from μ-ILEDs to the μ-IPD (i.e., that flows through the encapsulation materials without being scattered by the surrounding tissues), additional simulations used the configuration outlined above but with $\mu_a(\lambda)$ set to ~0.001 cm^{-1}. Here, almost all light at the tissue/probe interface passed through the tissue without backscatter or propagation back to the μ-IPD. This simulation method enabled quantified measurement of photoresponses that arise solely from direct light path. The averaged photoresponses (from six runs of simulation) indicated that the direct light path contribution is at least five orders of magnitude lower than that from backscattered light.

$rStO_2$ data analysis and calculation

Data analysis involved a commercial software package in MATLAB. Separation of the characteristic high and low output levels (in the form of ADC values) via a local minimal and maxima finding algorithm, followed by spline interpolation and down-sampling by a factor of 10, yielded data for two wavelengths. Optical densities as a function of time [OD(t)] are defined as

$$\mathrm{OD}(\lambda, t) = -\ln\left(I_\mathrm{t}(\lambda) \Big/ I_0(\lambda) \right) \quad (4)$$

where $I_\mathrm{t}(\lambda)$ is the time-dependent signal intensity and $I_0(\lambda)$ is the initial value, which were computed for both wavelengths (λ_1 and λ_2, green and red in this case). Other data processing of OD(λ, t) included linear detrending to remove the slow drifts and zero-lag digital Butterworth filtering with a low-pass cutoff frequency at 0.4 Hz to remove high-frequency noise (with respect to typical hemodynamics). Calculation of $\Delta[HbO_2]$ and Δ[Hb] followed from the modified Lambert-Beer law for diffusive media (*54*)

$$\begin{bmatrix} \Delta[\mathrm{HbO_2}](t) \\ \Delta[\mathrm{Hb}](t) \end{bmatrix} = \frac{1}{\rho} \begin{bmatrix} \varepsilon_{\mathrm{HbO_2}}(\lambda_1) \cdot \mathrm{DPF}(\lambda_1) & \varepsilon_{\mathrm{Hb}}(\lambda_1) \cdot \mathrm{DPF}(\lambda_1) \\ \varepsilon_{\mathrm{HbO_2}}(\lambda_2) \cdot \mathrm{DPF}(\lambda_2) & \varepsilon_{\mathrm{Hb}}(\lambda_2) \cdot \mathrm{DPF}(\lambda_2) \end{bmatrix}^{-1} \times \begin{bmatrix} \mathrm{OD}(\lambda_1, t) \\ \mathrm{OD}(\lambda_2, t) \end{bmatrix} \quad (5)$$

where ρ is the interoptode distance and DPF(λ) is the differential pathlength factor at the wavelength of interest. $\varepsilon(\lambda)$ of HbO_2 and Hb are available from previous reports (*27*, *55*). The DPF(λ) were estimated assuming an infinite geometry and derived as the following equation (*56*), with $\mu_s(\lambda)$ and $\mu_a(\lambda)$ extrapolated from (*57*)

$$\mathrm{DPF} = \frac{\sqrt{3\mu_s}}{2\sqrt{\mu_a}} \quad (6)$$

Approximations of the initial $[\mathrm{Hb}]_t$ (0.1 mM) and $rStO_2$ (at t = 0, 60%) (*56*) in the brain tissues of mice under ambient atmosphere enabled calculation of $rStO_2$ as a function of time for the in vivo experiments via the following equation

$$\mathrm{rStO_2}(t) = \frac{[\mathrm{HbO_2}](t)}{[\mathrm{HbO_2}](t) + [\mathrm{Hb}](t)} = \frac{[\mathrm{Hb}]_t(t=0) \cdot \mathrm{rStO_2}(t=0) + \Delta[\mathrm{HbO_2}](t)}{([\mathrm{Hb}]_t(t=0) \cdot \mathrm{rStO_2}(t=0) + \Delta[\mathrm{HbO_2}](t)) + ([\mathrm{Hb}]_t(t=0) \cdot (1 - \mathrm{rStO_2}(t=0)) + \Delta[\mathrm{Hb}](t))} \quad (7)$$

MicroCT imaging

Mice with subdermally implanted oximeters in the striatum were anesthetized in an induction chamber with 3% isoflurane in O_2 and

transferred to a dedicated imaging bed with isoflurane delivered via nose cone at 1 to 2%. The animals were then placed in the prone position with head immobilized with ear and tooth bars, and respiratory signals were monitored using a digital system (Mediso USA, Boston, MA). A preclinical microCT imaging system (nanoScan PET/CT, Mediso USA, Boston, MA) acquired images with the following parameters: ×2.2 magnification, <60-μm focal spot, 1 × 1 binning with 720 projection views over a full circle by using 70 kVp/520 μA with an exposure time of 300 ms. The projection data were reconstructed with a voxel size of 34 μm using filtered (Butterworth filter) back-projection software from Mediso. The reconstructed data were visualized and segmented in Amira 6.5 (FEI, Houston, TX).

SUPPLEMENTARY MATERIALS

Supplementary material for this article is available at http://advances.sciencemag.org/cgi/content/full/5/3/eaaw0873/DC1

Fig. S1. Scheme of the fabrication steps of the dual-layered wireless, battery-free oximeters.
Fig. S2. Scheme of wireless oximeters with different designs of injectable filaments.
Fig. S3. Optical images of the tip end of injectable filaments of wireless oximeters.
Fig. S4. Photographs of wireless oximeters with battery-powered electronic modules.
Fig. S5. Photograph of a battery-free, fully implantable, wireless oximeter on a balance.
Fig. S6. Ratio of extinction coefficients of HbO_2 and Hb.
Fig. S7. Scheme of the epitaxial stack of GaAs wafers used for the fabrication of μ-IPDs.
Fig. S8. Scheme and pseudocolored SEM image of GaAs-based μ-IPDs.
Fig. S9. Characterizations of μ-IPD and μ-ILEDs.
Fig. S10. Monte Carlo simulation results.
Fig. S11. Scheme of the experimental arena circumflexed with antenna for wireless power supply.
Fig. S12. Transmittance spectra of mouse scalp collected by a fiber optic spectrometer.
Fig. S13. Fluctuations in output signals ($\Delta I/I$) of the wireless, battery-free oximeters over time.
Fig. S14. Absorption spectra of five artificial blood solutions with various combinations of oxyhemoglobin, deoxyhemoglobin, and metHb.
Fig. S15. Raw data of $rStO_2$ collected by wireless, battery-powered oximetry implants in the tissue region near femoral artery of anesthetized rats.
Fig. S16. Surgical steps of the subdermal implantation of wireless, battery-free oximeters in mouse brain.
Fig. S17. Wireless oximetry data on mice with subdermally implanted, battery-free devices in the brain.
Fig. S18. Photographs of freely moving mice with brain-implanted oximeter filaments with connectors for the integration with battery-powered electronics.
Fig. S19. Weight changes of three mice after subdermal brain surgery with wireless, battery-free oximetry implants.
Table S1. Data transmission of the wireless, battery-free oximeters before and after subdermal implantation.
Movie S1. A wireless, battery-free, fully implantable oximeter with illuminating μ-ILEDs.

REFERENCES AND NOTES

1. S. Fantini, A. Sassaroli, Near-infrared optical mammography for breast cancer detection with intrinsic contrast. *Ann. Biomed. Eng.* **40**, 398–407 (2012).
2. A. Shmuel, M. Augath, A. Oeltermann, N. K. Logothetis, Negative functional MRI response correlates with decreases in neuronal activity in monkey visual area V1. *Nat. Neurosci.* **9**, 569–577 (2006).
3. J.-N. Liu, W. Bu, J. Shi, Chemical design and synthesis of functionalized probes for imaging and treating tumor hypoxia. *Chem. Rev.* **117**, 6160–6224 (2017).
4. H. W. Hopf, M. D. Rollins, Wounds: An overview of the role of oxygen. *Antioxid. Redox Signal.* **9**, 1183–1192 (2007).
5. A. Parpaleix, Y. G. Houssen, S. Charpak, Imaging local neuronal activity by monitoring PO_2 transients in capillaries. *Nat. Med.* **19**, 241–246 (2013).
6. B. Epel, H. J. Halpern, In vivo pO_2 imaging of tumors: Oxymetry with very low-frequency electron paramagnetic resonance. *Methods Enzymol.* **564**, 501–527 (2015).
7. S. Liu, S. J. Shah, L. J. Wilmes, J. Feiner, V. D. Kodibagkar, M. F. Wendland, R. P. Mason, N. Hylton, H. W. Hopf, M. D. Rollins, Quantitative tissue oxygen measurement in multiple organs using ^{19}F MRI in a rat model. *Magn. Reson. Med.* **66**, 1722–1730 (2011).
8. D. G. Lyons, A. Parpaleix, M. Roche, S. Charpak, Mapping oxygen concentration in the awake mouse brain. *eLife* **5**, e12024 (2016).
9. A. Ledo, C. F. Lourenço, J. Laranjinha, G. A. Gerhardt, R. M. Barbosa, Combined in vivo amperometric oximetry and electrophysiology in a single sensor: A tool for epilepsy research. *Anal. Chem.* **89**, 12383–12390 (2017).
10. D. L. Robinson, M. L. A. V. Heien, R. M. Wightman, Frequency of dopamine concentration transients increases in dorsal and ventral striatum of male rats during introduction of conspecifics. *J. Neurosci.* **22**, 10477–10486 (2002).
11. T.-i. Kim, J. G. McCall, Y. H. Jung, X. Huang, E. R. Siuda, Y. Li, J. Song, Y. M. Song, H. A. Pao, R.-H. Kim, C. Lu, S. D. Lee, I.-S. Song, G. Shin, R. Al-Hasani, S. Kim, M. P. Tan, Y. Huang, F. G. Omenetto, J. A. Rogers, M. R. Bruchas, Injectable, cellular-scale optoelectronics with applications for wireless optogenetics. *Science* **340**, 211–216 (2013).
12. J.-W. Jeong, J. G. McCall, G. Shin, Y. Zhang, R. Al-Hasani, M. Kim, S. Li, J. Y. Sim, K.-I. Jang, Y. Shi, D. Y. Hong, Y. Liu, G. P. Schmitz, L. Xia, Z. He, P. Gamble, W. Z. Ray, Y. Huang, M. R. Bruchas, J. A. Rogers, Wireless optofluidic systems for programmable in vivo pharmacology and optogenetics. *Cell* **162**, 662–674 (2015).
13. S. I. Park, G. Shin, J. G. McCall, R. Al-Hasani, A. Norris, L. Xia, D. S. Brenner, K. N. Noh, S. Y. Bang, D. L. Bhatti, K.-I. Jang, S.-K. Kang, A. D. Mickle, G. Dussor, T. J. Price, R. W. Gereau IV, M. R. Bruchas, J. A. Rogers, Stretchable multichannel antennas in soft wireless optoelectronic implants for optogenetics. *Proc. Natl. Acad. Sci. U.S.A.* **113**, E8169–E8177 (2016).
14. G. Shin, A. M. Gomez, R. Al-Hasani, Y. R. Jeong, J. Kim, Z. Xie, A. Banks, S. M. Lee, S. Y. Han, C. J. Yoo, J.-L. Lee, S. H. Lee, J. Kurniawan, J. Tureb, Z. Guo, J. Yoon, S.-I. Park, S. Y. Bang, Y. Nam, M. C. Walicki, V. K. Samineni, A. D. Mickle, K. Lee, S. Y. Heo, J. G. McCall, T. Pan, L. Wang, X. Feng, T. Kim, J. K. Kim, Y. Li, Y. Huang, R. W. Gereau IV, J. S. Ha, M. R. Bruchas, J. A. Rogers, Flexible near-field wireless optoelectronics as subdermal implants for broad applications in optogenetics. *Neuron* **93**, 509–521.e3 (2017).
15. R. Al-Hasani, J. G. McCall, G. Shin, A. M. Gomez, G. P. Schmitz, J. M. Bernardi, C.-O. Pyo, S. I. Park, C. M. Marcinkiewcz, N. A. Crowley, M. J. Krashes, B. B. Lowell, T. L. Kash, J. A. Rogers, M. R. Bruchas, Distinct subpopulations of nucleus accumbens dynorphin neurons drive aversion and reward. *Neuron* **87**, 1063–1077 (2015).
16. S. I. Park, D. S. Brenner, G. Shin, C. D. Morgan, B. A. Copits, H. U. Chung, M. Y. Pullen, K. N. Noh, S. Davidson, S. J. Oh, J. Yoon, K.-I. Jang, V. K. Samineni, M. Norman, J. G. Grajales-Reyes, S. K. Vogt, S. S. Sundaram, K. M. Wilson, J. S. Ha, R. Xu, T. Pan, T.-i. Kim, Y. Huang, M. C. Montana, J. P. Golden, M. R. Bruchas, R. W. Gereau IV, J. A. Rogers, Soft, stretchable, fully implantable miniaturized optoelectronic systems for wireless optogenetics. *Nat. Biotechnol.* **33**, 1280–1286 (2015).
17. H. Zhang, J. A. Rogers, Recent advances in flexible inorganic light emitting diodes: From materials design to integrated optoelectronic platforms. *Adv. Opt. Mater.* **7**, 1800936 (2019).
18. L. Lu, P. Gutruf, L. Xia, D. L. Bhatti, X. Wang, A. Vazquez-Guardado, X. Ning, X. Shen, T. Sang, R. Ma, G. Pakeltis, G. Sobczak, H. Zhang, D.-o. Seo, M. Xue, L. Yin, D. Chanda, X. Sheng, M. R. Bruchas, J. A. Rogers, Wireless optoelectronic photometers for monitoring neuronal dynamics in the deep brain. *Proc. Natl. Acad. Sci. U.S.A.* **115**, E1374–E1383 (2018).
19. D. W. Green, G. Kunst, Cerebral oximetry and its role in adult cardiac, non-cardiac surgery and resuscitation from cardiac arrest. *Anaesthesia* **72**, 48–57 (2017).
20. J. M. Murkin, M. Arango, Near-infrared spectroscopy as an index of brain and tissue oxygenation. *Br. J. Anaesth.* **103**, i3–i13 (2009).
21. S. Soares, B. V. Atallah, J. J. Paton, Midbrain dopamine neurons control judgment of time. *Science* **354**, 1273–1277 (2016).
22. C. K. Kim, S. J. Yang, N. Pichamoorthy, N. P. Young, I. Kauvar, J. H. Jennings, T. N. Lerner, A. Berndt, S. Y. Lee, C. Ramakrishan, T. J. Davidson, M. Inoue, H. Bito, K. Deisseroth, Simultaneous fast measurement of circuit dynamics at multiple sites across the mammalian brain. *Nat. Methods* **13**, 325–328 (2016).
23. D.-H. Kim, J. Viventi, J. J. Amsden, J. Xiao, L. Vigeland, Y.-S. Kim, J. A. Blanco, B. Panilaitis, E. S. Frechette, D. Contreras, D. L. Kaplan, F. G. Omenetto, Y. Huang, K.-C. Hwang, M. R. Zakin, B. Litt, J. A. Rogers, Dissolvable films of silk fibroin for ultrathin conformal bio-integrated electronics. *Nat. Mater.* **9**, 511–517 (2010).
24. L. Luan, X. Wei, Z. Zhao, J. J. Siegel, O. Potnis, C. A. Tuppen, S. Lin, S. Kazmi, R. A. Fowler, S. Holloway, A. K. Dunn, R. A. Chitwood, C. Xie, Ultraflexible nanoelectronic probes form reliable, glial scar–free neural integration. *Sci. Adv.* **3**, e1601966 (2017).
25. P. Gutruf, V. Krishnamurthi, A. Vázquez-Guardado, A. Banks, C.-J. Su, Y. Xu, C. R. Haney, E. A. Waters, I. Kandela, S. R. Krishnan, T. Ray, J. P. Leshock, Y. Huang, D. Chanda, J. A. Rogers, Fully implantable optoelectronic systems for battery-free, multimodal operation in neuroscience research. *Nat. Electron.* **1**, 652–660 (2018).
26. J. A. Fan, W.-H. Yeo, Y. Su, Y. Hattori, W. Lee, S.-Y. Jung, Y. Zhang, Z. Liu, H. Cheng, L. Falgout, M. Bajema, T. Coleman, D. Gregoire, R. J. Larsen, Y. Huang, J. A. Rogers, Fractal design concepts for stretchable electronics. *Nat. Commun.* **5**, 3266 (2014).
27. P. Scott, Oregon Medical Laser Center (1999); http://omlc.ogi.edu/spectra/hemoglobin.
28. J. Kim, G. A. Salvatore, H. Araki, A. M. Chiarelli, Z. Xie, A. Banks, X. Sheng, Y. Liu, J. W. Lee, K.-I. Jang, S. Y. Heo, K. Cho, H. Luo, B. Zimmerman, J. Kim, L. Yan, X. Feng, S. Xu, M. Fabiani, G. Gratton, Y. Huang, U. Paik, J. A. Rogers, Battery-free, stretchable optoelectronic systems for wireless optical characterization of the skin. *Sci. Adv.* **2**, e1600418 (2016).

29. J. Kim, P. Gutruf, A. M. Chiarelli, S. Y. Heo, K. Cho, Z. Xie, A. Banks, S. Han, K.-I. Jang, J. W. Lee, K.-T. Lee, X. Feng, Y. Huang, M. Fabiani, G. Gratton, U. Paik, J. A. Rogers, Miniaturized battery-free wireless systems for wearable pulse oximetry. *Adv. Funct. Mater.* **27**, 1604373 (2017).
30. A. Mustari, N. Nakamura, S. Kawauchi, S. Sato, M. Sato, I. Nishidate, RGB camera-based imaging of cerebral tissue oxygen saturation, hemoglobin concentration, and hemodynamic spontaneous low-frequency oscillations in rat brain following induction of cortical spreading depression. *Biomed. Opt. Express* **9**, 933–951 (2018).
31. B. M. Raabe, J. E. Artwohl, J. E. Purcell, J. Lovaglio, J. D. Fortman, Effects of weekly blood collection in C57BL/6 mice. *J. Am. Assoc. Lab. Anim. Sci.* **50**, 680–685 (2011).
32. A. Devor, A. K. Dunn, M. L. Andermann, I. Ulbert, D. A. Boas, A. M. Dale, Coupling of total hemoglobin concentration, oxygenation, and neural activity in rat somatosensory cortex. *Neuron* **39**, 353–359 (2003).
33. S. Hyttel-Sorensen, T. W. Hessel, G. Greisen, Peripheral tissue oximetry: Comparing three commercial near-infrared spectroscopy oximeters on the forearm. *J. Clin. Monit. Comput.* **28**, 149–155 (2014).
34. J. Yao, L. V. Wang, Photoacoustic brain imaging: From microscopic to macroscopic scales. *Neurophotonics* **1**, 011003 (2014).
35. L. M. Smith, J. Varagic, L. M. Yamaleyeva, Photoacoustic imaging for the detection of hypoxia in the rat femoral artery and skeletal muscle microcirculation. *Shock* **46**, 527–530 (2016).
36. C. D. Kurth, W. J. Levy, J. McCann, Near-infrared spectroscopy cerebral oxygen saturation thresholds for hypoxia-ischemia in piglets. *J. Cereb. Blood Flow Metab.* **22**, 335–341 (2002).
37. L. M. Smith, R. W. Barbee, K. R. Ward, R. N. Pittman, Decreased supply-dependent oxygen consumption in the skeletal muscle of the spontaneously hypertensive rat during acute hypoxia. *Shock* **25**, 618–624 (2006).
38. G. Vretzakis, S. Georgopoulou, K. Stamoulis, G. Stamatiou, K. Tsakiridis, P. Zarogoulidis, N. Katsikogianis, I. Kougioumtzi, N. Machairiotis, T. Tsiouda, A. Mpakas, T. Beleveslis, A. Koletas, S. N. Siminelakis, K. Zarogoulidis, Cerebral oximetry in cardiac anesthesia. *J. Thorac. Dis.* **6**, S60–S69 (2014).
39. C. M. Lochner, Y. Khan, A. Pierre, A. C. Arias, All-organic optoelectronic sensor for pulse oximetry. *Nat. Commun.* **5**, 5745 (2014).
40. T. Yokota, P. Zalar, M. Kaltenbrunner, H. Jinno, N. Matsuhisa, H. Kitanosako, Y. Tachibana, W. Yukita, M. Koizumi, T. Someya, Ultraflexible organic photonic skin. *Sci. Adv.* **2**, e1501856 (2016).
41. Y. Khan, D. Han, A. Pierre, J. Ting, X. Wang, C. M. Lochner, G. Bovo, N. Yaacobi-Gross, C. Newsome, R. Wilson, A. C. Arias, A flexible organic reflectance oximeter array. *Proc. Natl. Acad. Sci. U.S.A.* **115**, E11015–E11024 (2018).
42. L. Xiang, P. Yu, M. Zhang, J. Hao, Y. Wang, L. Zhu, L. Dai, L. Mao, Platinized aligned carbon nanotube-sheathed carbon fiber microelectrodes for in vivo amperometric monitoring of oxygen. *Anal. Chem.* **86**, 5017–5023 (2014).
43. S. Ogawa, T. M. Lee, A. R. Kay, D. W. Tank, Brain magnetic resonance imaging with contrast dependent on blood oxygenation. *Proc. Natl. Acad. Sci. U.S.A.* **87**, 9868–9872 (1990).
44. E. Jonckers, D. Shah, J. Hamaide, M. Verhoye, A. van der Linden, The power of using functional fMRI on small rodents to study brain pharmacology and disease. *Front. Pharmacol.* **6**, 231 (2015).
45. M.-L. Li, J.-T. Oh, X. Xie, G. Ku, W. Wang, C. Li, G. Lungu, G. Stoica, L. V. Wang, Simultaneous molecular and hypoxia imaging of brain tumors in vivo using spectroscopic photoacoustic tomography. *Proc. IEEE* **96**, 481–489 (2008).
46. Y. Tomioka, S. Enomoto, J. Gu, A. Kaneko, I. Saito, Y. Inoue, T. Woo, I. Koshima, K. Yoshimura, T. Someya, M. Sekino, Multipoint tissue circulation monitoring with a flexible optical probe. *Sci. Rep.* **7**, 9643 (2017).
47. S. J. Lin, M.-D. Nguyen, C. Chen, S. Colakoglu, M. S. Curtis, A. M. Tobias, B. T. Lee, Tissue oximetry monitoring in microsurgical breast reconstruction decreases flap loss and improves rate of flap salvage. *Plast. Reconstr. Surg.* **127**, 1080–1085 (2011).
48. L. R. Walton, N. G. Boustead, S. Carroll, R. M. Wightman, Effects of glutamate receptor activation on local oxygen changes. *ACS Chem. Neurosci.* **8**, 1598–1608 (2017).
49. E. von Borell, J. Langbein, G. Després, S. Hansen, C. Leterrier, J. Marchant-Forde, R. Marchant-Forde, M. Minero, E. Mohr, A. Prunier, D. Valance, I. Veissier, Heart rate variability as a measure of autonomic regulation of cardiac activity for assessing stress and welfare in farm animals—A review. *Physiol. Behav.* **92**, 293–316 (2007).
50. J. D. Harvey, P. V. Jena, H. A. Baker, G. H. Zerze, R. M. Williams, T. V. Galassi, D. Roxbury, J. Mittal, D. A. Heller, A carbon nanotube reporter of miRNA hybridization events in vivo. *Nat. Biomed. Eng.* **1**, 0041 (2017).
51. T.-i. Kim, M. J. Kim, Y. H. Jung, H. W. Jang, C. Dagdeviren, H. A. Pao, S. J. Cho, A. Carlson, K. J. Yu, A. Ameen, H.-j. Chung, S. H. Jin, Z. Ma, J. A. Rogers, Thin film receiver materials for deterministic assembly by transfer printing. *Chem. Mater.* **26**, 3502–3507 (2014).
52. S. L. Jacques, Optical properties of biological tissues: A review. *Phys. Med. Biol.* **58**, R37–R61 (2013).
53. Y. Song, S. Garcia, Y. Frometa, J. C. Ramella-Roman, M. Soltani, M. Almadi, J. J. Riera, W.-C. Lin, Quantitative assessment of hemodynamic and structural characteristics of in vivo brain tissue using total diffuse reflectance spectrum measured in a non-contact fashion. *Biomed. Opt. Express* **8**, 78–103 (2017).
54. D. T. Delpy, M. Cope, P. van der Zee, S. Arridge, S. Wray, J. Wyatt, Estimation of optical pathlength through tissue from direct time of flight measurement. *Phys. Med. Biol.* **33**, 1433–1442 (1988).
55. W. G. Zijlstra, A. Buursma, W. P. Meeuwsen-van der Roest, Absorption spectra of human fetal and adult oxyhemoglobin, de-oxyhemoglobin, carboxyhemoglobin, and methemoglobin. *Clin. Chem.* **37**, 1633–1638 (1991).
56. D. Piao, R. L. Barbour, H. L. Graber, D. C. Lee, On the geometry dependence of differential pathlength factor for near-infrared spectroscopy. I. Steady-state with homogeneous medium. *J. Biomed. Opt.* **20**, 105005 (2015).
57. D. J. Cuccia, D. Abookasis, R. D. Frostig, B. J. Tromberg, Quantitative in vivo imaging of tissue absorption, scattering, and hemoglobin concentration in rat cortex using spatially modulated structured light, in *In Vivo Optical Imaging of Brain Function*, R. D. Frostig, Ed. (CRC Press/Taylor & Francis, ed. 2, 2009), chap. 12.

Acknowledgments: We thank A. Birkha for processing the microCT images and I. Stepien for providing weight data of mice with subdermal oximeter implants. **Funding:** This research was supported by the Center for Bio-Integrated Electronics at Northwestern University. The work used the Northwestern University Micro/Nano Fabrication Facility (NUFAB), which is partially supported by the Soft and Hybrid Nanotechnology Experimental (SHyNE) Resource (NSF ECCS-1542205), the Materials Research Science and Engineering Center (DMR-1720139), the State of Illinois, and Northwestern University and facilities at Frederick Seitz Materials Research Laboratory for Advanced Science and Technology at the University of Illinois at Urbana-Champaign. This work was supported by the Developmental Therapeutics Core at Northwestern University and the Robert H. Lurie Comprehensive Cancer Center support grant (NCI CA060553). **Author contributions:** H. Zhang, P.G., and J.A.R. designed the research, analyzed the data, and led in writing the manuscript. H. Zhang and P.G. fabricated and characterized the devices with the assistance from X.Z., L.L., Q.G., C.X., Y.W., H.Zhao, and X.N. H. Zhang, P.G., K.M., M.C.M., A.N., W.B., I.K., and R.W.G. designed and performed the in vivo experiments. A.M.C. developed the algorithm and performed the tissue oximetry data analysis. A.V.-G. and D.C. designed and performed optical simulation. C.R.H. performed the microCT imaging of mice with subdermal oximeter implants. All authors commented on the manuscript. **Competing interests:** The authors declare that they have no competing interests. **Data and materials availability:** All data needed to evaluate the conclusion in this paper are present in the paper and/or Supplementary Materials. Additional data related to this paper may be requested from the authors.

Submitted 16 November 2018
Accepted 28 January 2019
Published 8 March 2019
10.1126/sciadv.aaw0873

Citation: H. Zhang, P. Gutruf, K. Meacham, M. C. Montana, X. Zhao, A. M. Chiarelli, A. Vázquez-Guardado, A. Norris, L. Lu, Q. Guo, C. Xu, Y. Wu, H. Zhao, X. Ning, W. Bai, I. Kandela, C. R. Haney, D. Chanda, R. W. Gereau, J. A. Rogers, Wireless, battery-free optoelectronic systems as subdermal implants for local tissue oximetry. *Sci. Adv.* **5**, eaaw0873 (2019).

Science Advances

Wireless, battery-free optoelectronic systems as subdermal implants for local tissue oximetry

Hao Zhang, Philipp Gutruf, Kathleen Meacham, Michael C. Montana, Xingyue Zhao, Antonio M. Chiarelli, Abraham Vázquez-Guardado, Aaron Norris, Luyao Lu, Qinglei Guo, Chenkai Xu, Yixin Wu, Hangbo Zhao, Xin Ning, Wubin Bai, Irawati Kandela, Chad R. Haney, Debashis Chanda, Robert W. Gereau IV and John A. Rogers

Sci Adv **5** (3), eaaw0873.
DOI: 10.1126/sciadv.aaw0873

Science Advances
AAAS

advances.sciencemag.org/cgi/content/full/5/3/eaaw0873/DC1

Supplementary Materials for

Wireless, battery-free optoelectronic systems as subdermal implants for local tissue oximetry

Hao Zhang, Philipp Gutruf, Kathleen Meacham, Michael C. Montana, Xingyue Zhao, Antonio M. Chiarelli, Abraham Vázquez-Guardado, Aaron Norris, Luyao Lu, Qinglei Guo, Chenkai Xu, Yixin Wu, Hangbo Zhao, Xin Ning, Wubin Bai, Irawati Kandela, Chad R. Haney, Debashis Chanda, Robert W. Gereau IV, John A. Rogers*

*Corresponding author. Email: jrogers@northwestern.edu.

Published 8 March 2019, *Sci. Adv.* **5**, eaaw0873 (2019)
DOI: 10.1126/sciadv.aaw0873

The PDF file includes:

Table S1. Data transmission of the wireless, battery-free oximeters before and after subdermal implantation.
Legend for movie S1

Other Supplementary Material for this manuscript includes the following:

(available at advances.sciencemag.org/cgi/content/full/5/3/eaaw0873/DC1)

Movie S1 (.mp4 format). A wireless, battery-free, fully implantable oximeter with illuminating μ-ILEDs.

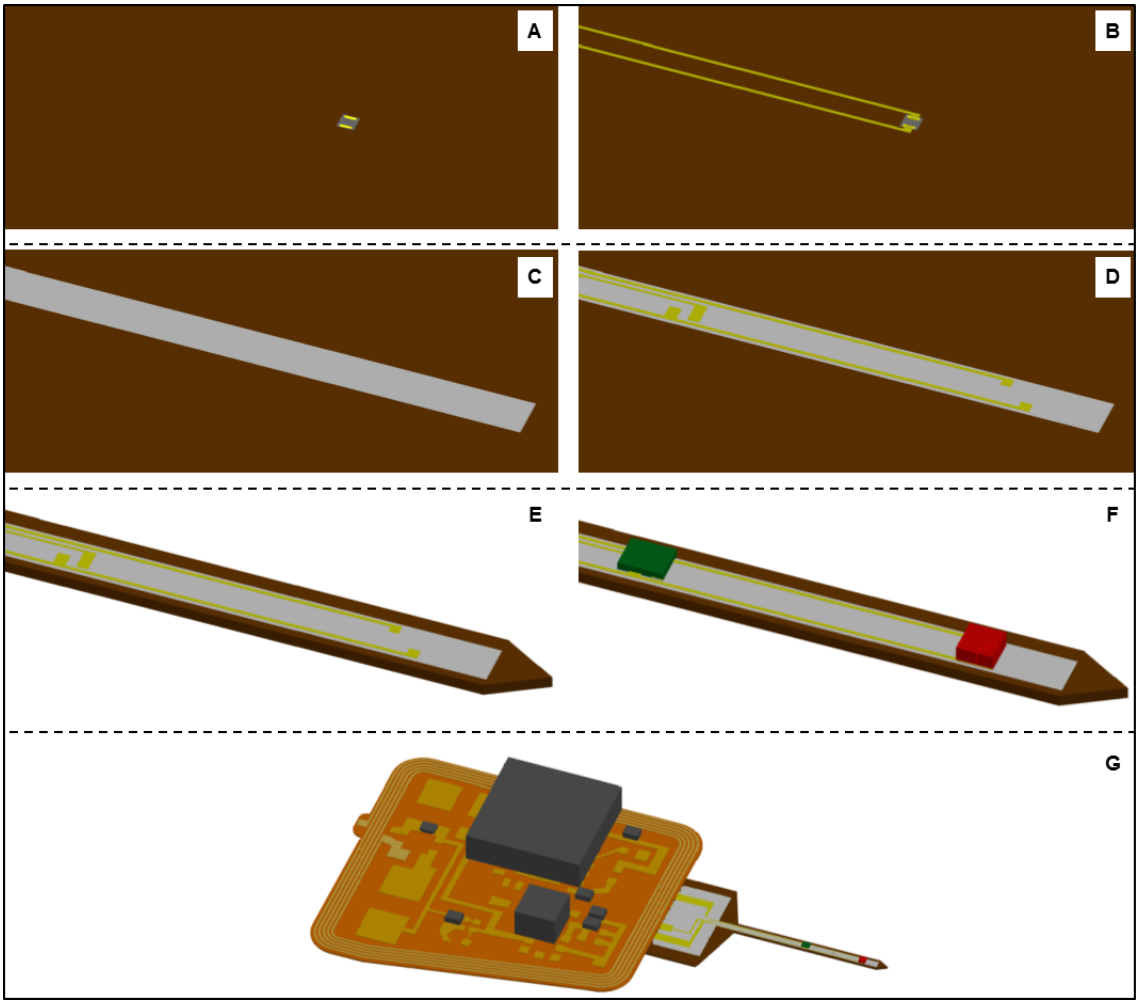

Fig. S1. Scheme of the fabrication steps of the dual-layered wireless, battery-free oximeters. (**A**) Micro-transfer printing of a μ-IPD on a 75 μm-thick PI substrate; (**B**) Deposition of first layer of Au/Cu interconnects for the μ-IPD; (**C**) Photopatterning of a 7 μm-thick SU–8 separation layer; (**D**) Deposition of the second layer of Au/Cu interconnects for the μ-ILEDs; (**E**) Cutting out the shape of injectable filaments by UV laser; (**F**) Micro-transfer printing and soldering of the μ-ILEDs; (**G**) Integration of the injectable filament and electronic module into a complete embodiment via low temperature reflow soldering. Note only part of the electronic components are shown in (G).

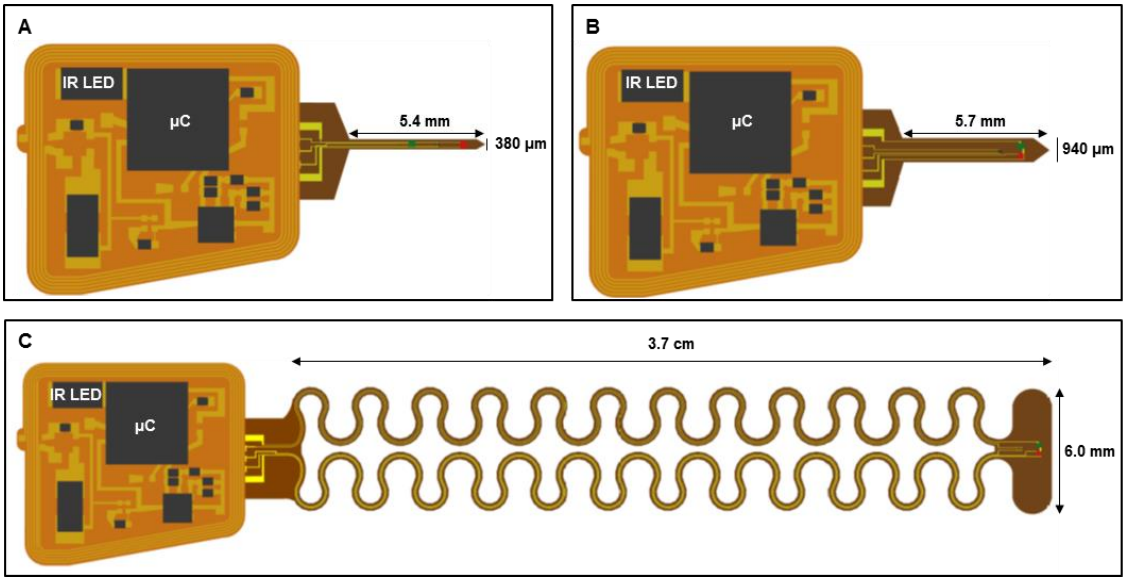

Fig. S2. Scheme of wireless oximeters with different designs of injectable filaments. (**A**) The dual-layered design with a sub-400 μm width for deep brain $rStO_2$ sensing of mice. The SU–8 separation layer is omitted for clarity; (**B**) The single-layered design for highly localized $rStO_2$ sensing in other tissue regions; (**C**) The stretchable design with serpentine-shaped interconnects.

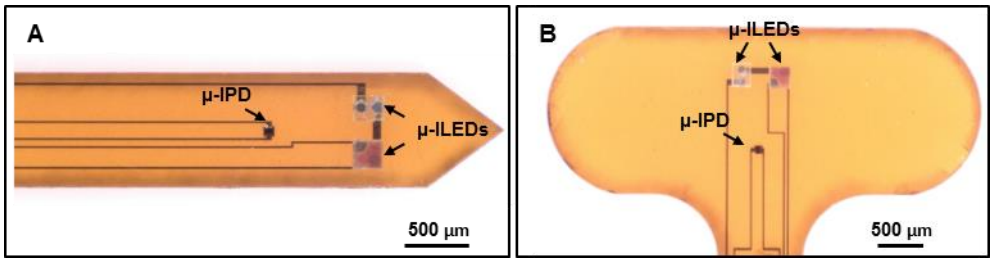

Fig. S3. Optical images of the tip end of injectable filaments of wireless oximeters. (**A**) Single-layered and (**B**) stretchable designs.

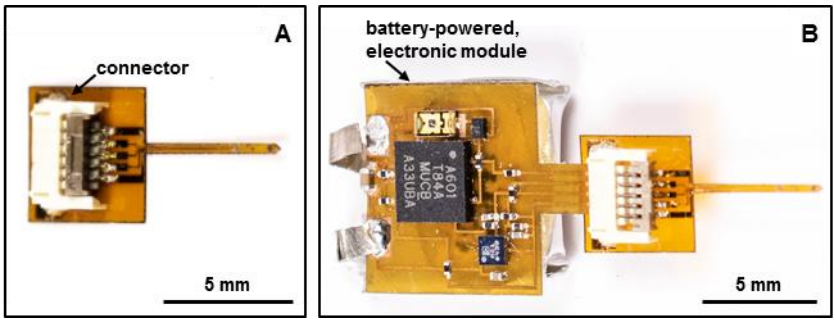

Fig. S4. Photographs of wireless oximeters with battery-powered electronic modules. (**A**) The filamentary sensing module with a back-flip connector; (**B**) A complete device embodiment with the detachable, battery-powered electronic module. (Photo credit: Philipp Gutruf, Northwestern University)

Fig. S5. Photograph of a battery-free, fully implantable, wireless oximeter on a balance. (Photo credit: Philipp Gutruf, Northwestern University)

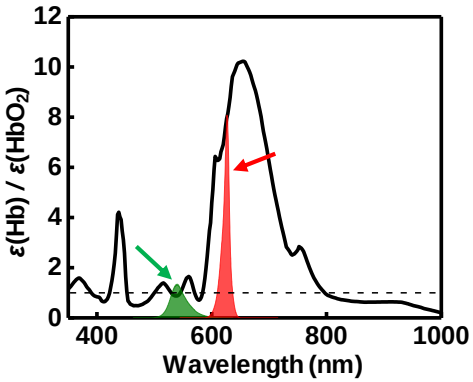

Fig. S6. Ratio of extinction coefficients of HbO_2 and Hb. Green and red shaded areas indicate the emission spectra of green and red μ-ILEDs, respectively. The dashed line corresponds to $\varepsilon(Hb) = \varepsilon(HbO_2)$.

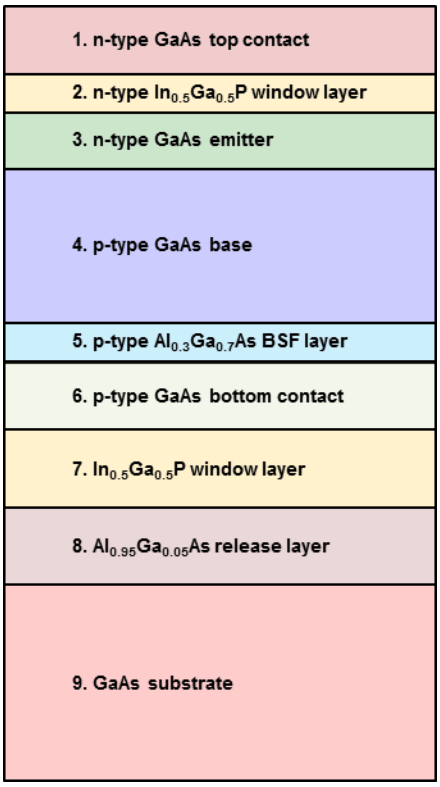

Fig. S7. Scheme of the epitaxial stack of GaAs wafers used for the fabrication of μ-IPDs. 1. n-type GaAs top contact, 100 nm, Te-doped, $>1\times10^{19}$ cm^{-3} and 100 nm, Si-doped, $\sim2\times10^{18}$ cm^{-3}; 2. n-type $In_{0.5}Ga_{0.5}P$ window layer, 25 nm, Si-doped, 2×10^{18} cm^{-3}; 3. n-type GaAs emitter layer, 100 nm, Si-doped, 2×10^{18} cm^{-3}; 4. p-type GaAs base layer, 2500 nm, Zn-doped, 1×10^{17} cm^{-3}; 5. p-type $Al_{0.3}Ga_{0.7}As$ back surface field (BSF) layer, 100 nm, Zn-doped, 5×10^{18} to 1×10^{19} cm^{-3}; 6. p-type GaAs bottom contact layer, 300 nm, Zn-doped, 5×10^{19} cm^{-3}; 7. $In_{0.5}Ga_{0.5}P$ window layer, 700 nm, no doping; 8. $Al_{0.95}Ga_{0.05}As$ release layer, 500 nm; 9. GaAs substrate.

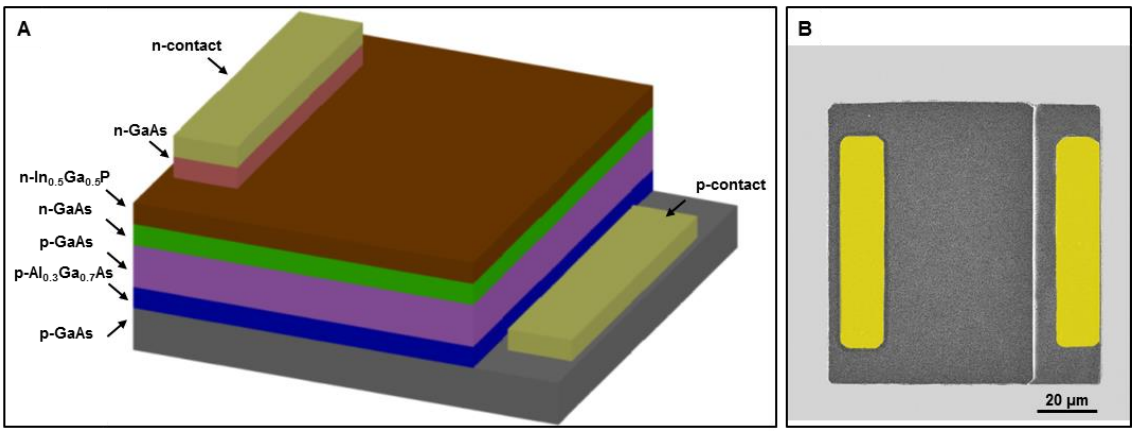

Fig. S8. Scheme and pseudocolored SEM image of GaAs-based μ-IPDs. The n- and p-contacts in (**B**) are shown in yellow color.

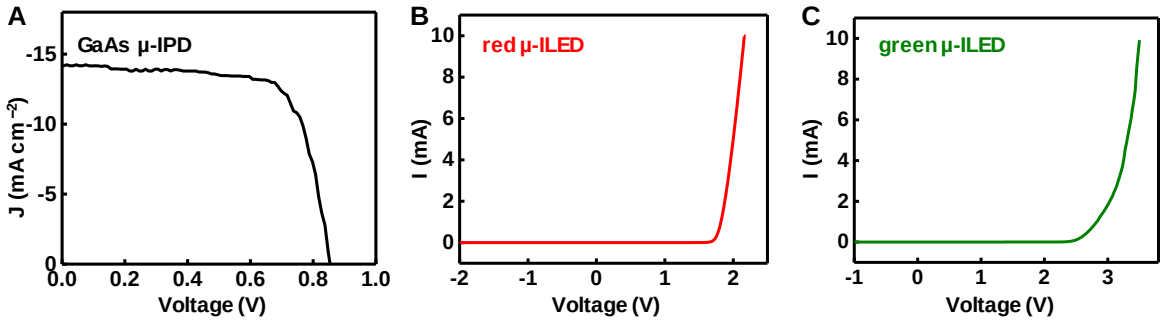

Fig. S9. Characterizations of μ-IPD and μ-ILEDs. (**A**) Current density versus voltage (J−V) curve of a GaAs μ-IPD under AM 1.5 G (100 mW cm^{-2}) illumination. (**B**, **C**) Current versus voltage (I−V) curves of red and green μ-ILEDs.

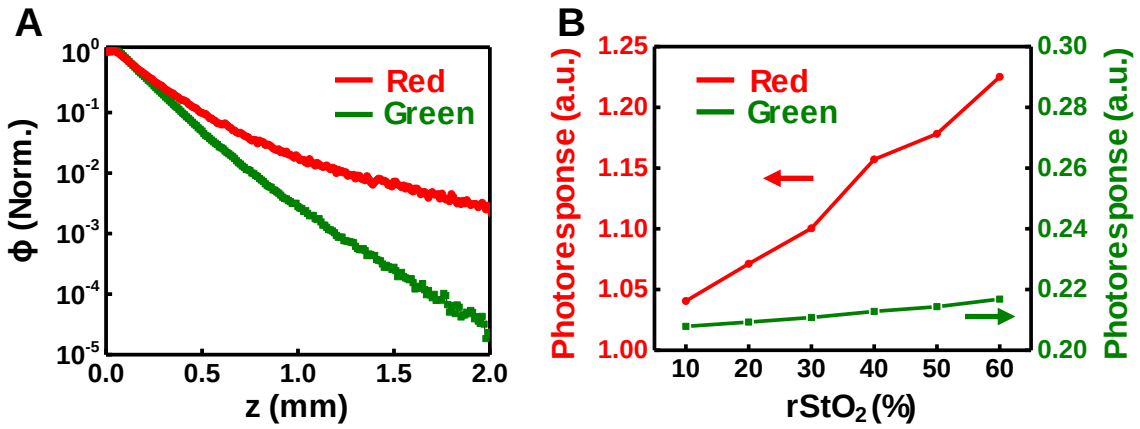

Fig. S10. Monte Carlo simulation results. (**A**) Normalized light intensities from red and green μ-ILEDs along z-axis and (**B**) Photoresponses of μ-IPD in response to red and green μ-ILEDs versus $rStO_2$.

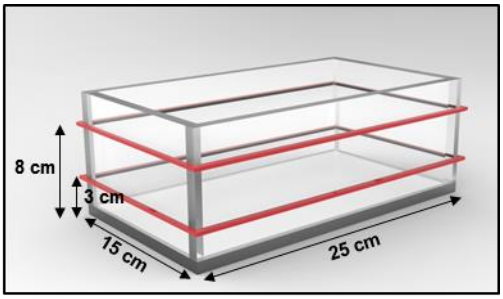

Fig. S11. Scheme of the experimental arena circumflexed with antenna for wireless power supply. The arena has dimensions (L×W×H = 25×15×10 cm) similar to a regular mouse home cage and is circumflexed with a dual loop antenna (indicated by red lines).

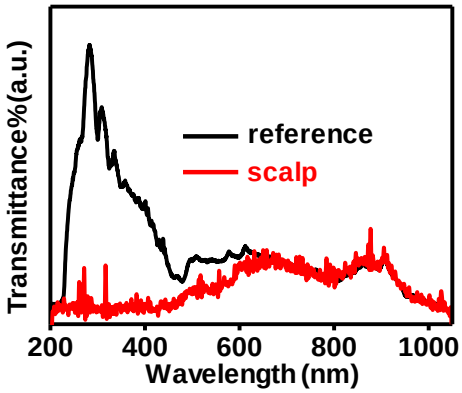

Fig. S12. Transmittance spectra of mouse scalp collected by a fiber optic spectrometer. The sample (labelled as "scalp") is enclosed in a plastic container and the plastic container serves as the "reference". The integration time for the measurements is set to keep the recorded transmittance of scalp and reference samples the same in the spectral band of ~700–1000 nm.

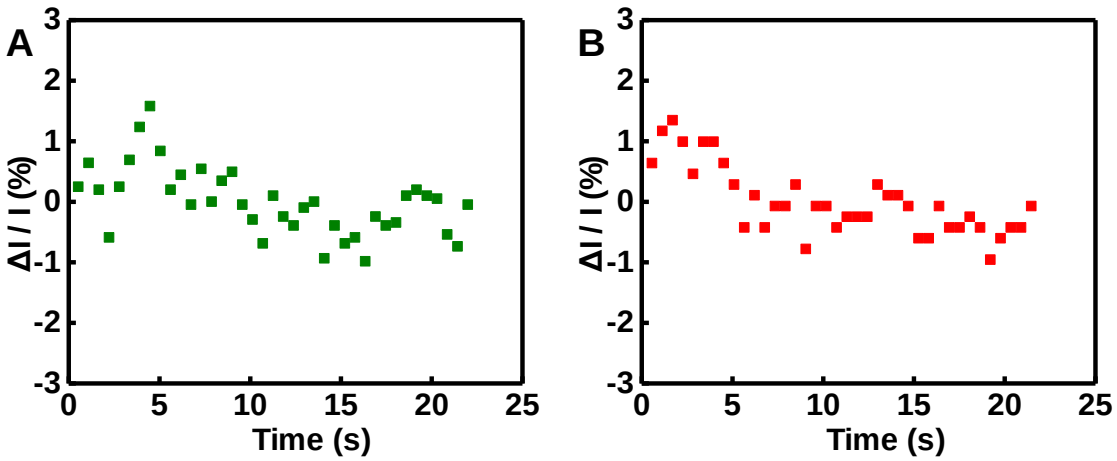

Fig. S13. Fluctuations in output signals (Δ*I*/*I*) of the wireless, battery-free oximeters over time. The fluctuation in output signals is defined as the variance between each recorded ADC value and the mean value, divided by the mean value. (**A**) and (**B**) show data related to green and red μ-ILEDs, respectively. The probe of wireless oximeters is immersed in solution 1 (commercial hemoglobin powder dissolved in PBS buffers, 25 g/L) placed in an experimental arena with the dimensions of a mouse home cage and with the RF power input of 4 W.

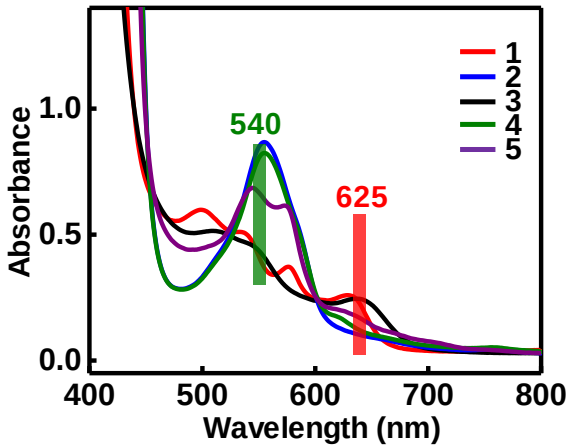

Fig. S14. Absorption spectra of five artificial blood solutions with various combinations of oxyhemoglobin, deoxyhemoglobin, and metHb. The concentration of total hemoglobin in each solution for the UV-visible spectroscopic measurements is 1.25 g/L. The green and red bars indicate the dominant emission wavelengths of the green (540 nm) and red (625 nm) μ-ILEDs.

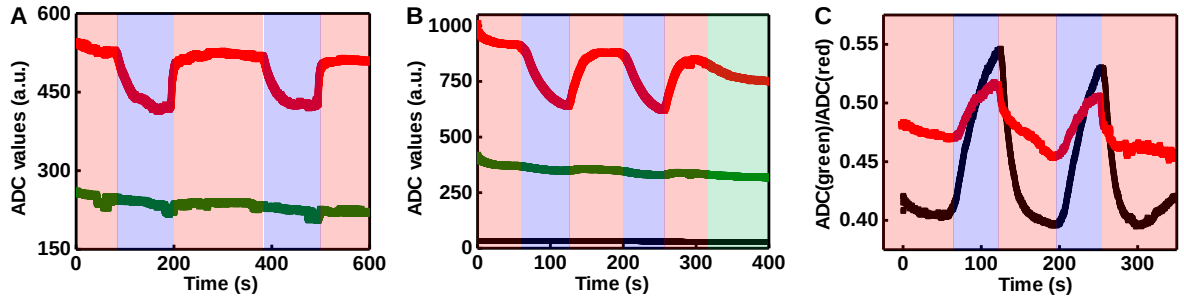

Fig. S15. Raw data of $rStO_2$ collected by wireless, battery-powered oximetry implants in the tissue region near femoral artery of anesthetized rats. (**A**, **B**) Temporal changes in raw ADC values of output photoresponses related to green (green curves) and red (red curves) μ-ILEDs in response to FiO_2 challenges. The black curve in (B) corresponds to baseline data (related to the dark current of the μ-IPD) recorded when both μ-ILEDs are off. (**C**) Changes in the ratio of ADC values associated with green and red μ-ILEDs when implanting the device right underneath the femoral artery (0.5–1 mm, black curve) and in deep tissue (2–4 mm, red curve), highlighting the sensing capability of highly localized $rStO_2$. For all experiments, the rats are exposed to different FiO_2 though a nose cone (red blocks: hyperoxia: pure O_2 with 2% isoflurane; purple blocks: hypoxia: 8% O_2; green blocks: normoxia: ambient atmosphere).

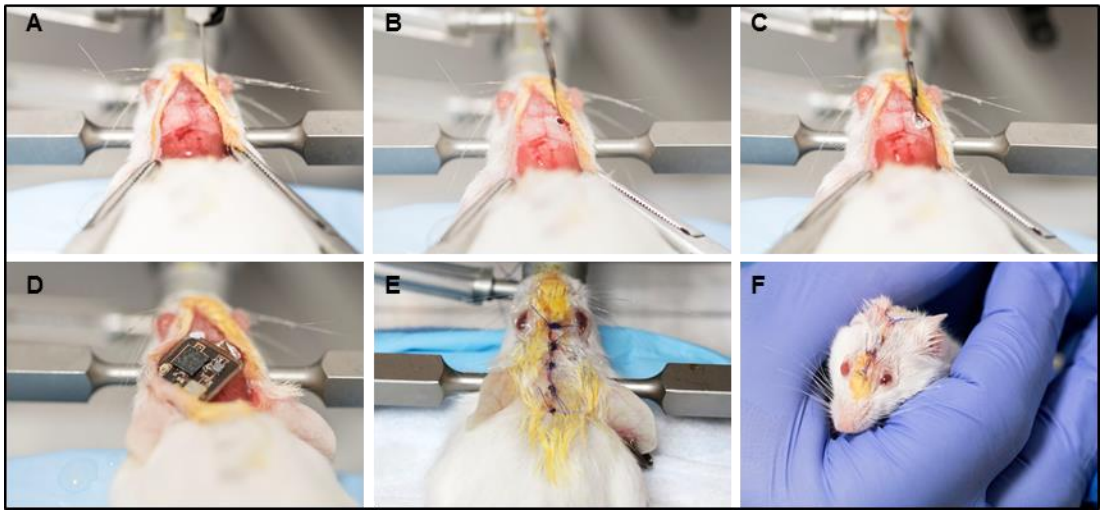

Fig. S16. Surgical steps of the subdermal implantation of wireless, battery-free oximeters in mouse brain. (**A**) Fixing the head of an anesthetized mouse on the stereotax followed by scalp opening. (**B**) Opening a hole with a drill bit in the skull for filament implantation. (**C**) Lowering the injectable filament into the hole and fixing it with dental cement or cyanoacrylate. (**D**) Bending the electronic module and laying it on the skull. (**E**, **F**) Closing scalp with bioresorbable sutures. (Photo credit: Philipp Gutruf, Northwestern University)

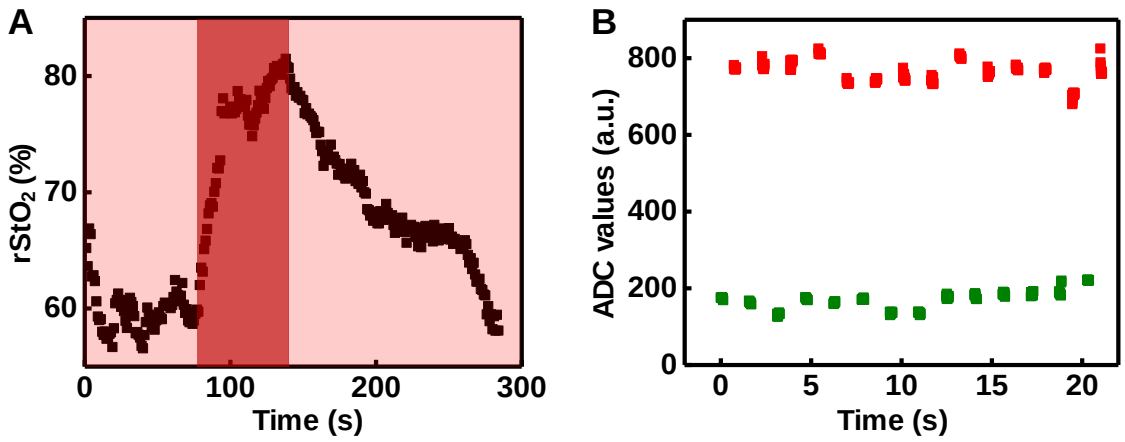

Fig. S17. Wireless oximetry data on mice with subdermally implanted, battery-free devices in the brain. (**A**) Temporal changes in estimated $rStO_2$ of an anesthetized mouse experiencing normal anesthesia gas mixture (O_2 with 2% isoflurane, indicated by light red blocks) or increased flow rates of O_2 supply (indicated by dark red block) via a nose cone; (**B**) Temporal raw ADC values of output photoresponses related to green (green squares) and red (red squares) wavelengths from subdermal, wireless oximetry implants in a freely-moving mouse at ambient atmosphere.

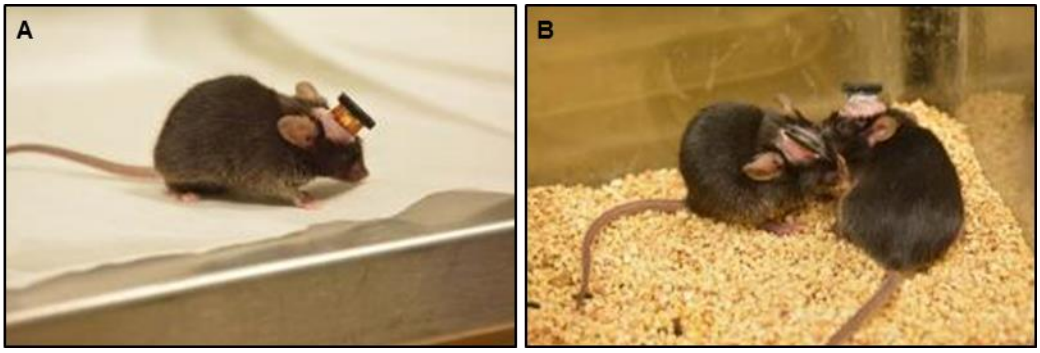

Fig. S18. Photographs of freely moving mice with brain-implanted oximeter filaments with connectors for the integration with battery-powered electronics. (Photo credit: Michael C. Montana, Washington University School of Medicine)

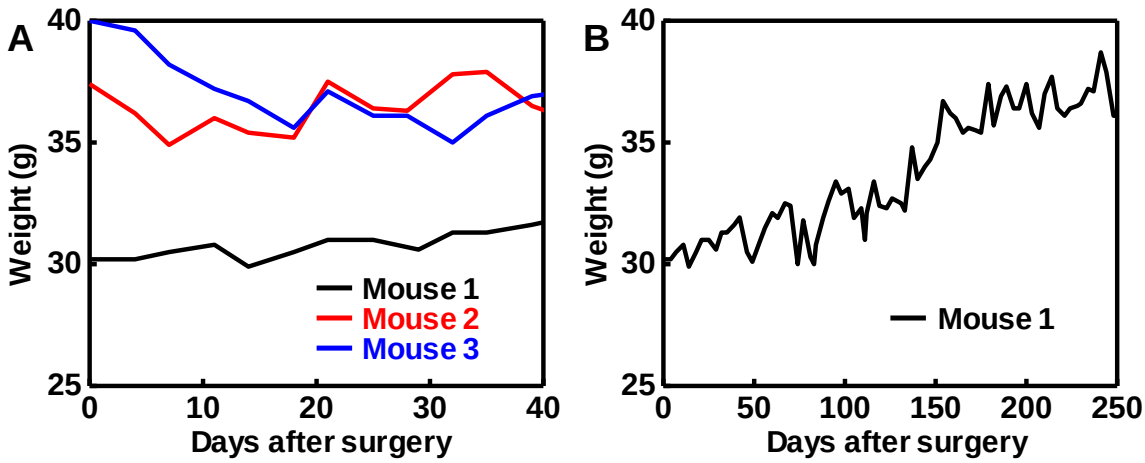

Fig. S19. Weight changes of three mice after subdermal brain surgery with wireless, battery-free oximetry implants.

Table S1. Data transmission of the wireless, battery-free oximeters before and after subdermal implantation. Encoding: NEC, Code: 0 (12 bits), Sequential timing with timing tolerance of 50 μs. Numbers in red and black colors correspond to ON and OFF states.

Timing before implantation (μs)	Timing after implantation (μs)
8850	8800
4350	4350
600	650
500	500
600	550
500	550
650	650
500	500
600	600
500	500
650	650
450	500
650	600
500	550
600	600
500	500
650	600
500	500

600	600
500	500
600	600
500	550
650	600
500	500
600	650
500	500
650	600

Movie S1. A wireless, battery-free, fully implantable oximeter with illuminating μ-ILEDs.

(Movie Credit: Philipp Gutruf, Northwestern University)